RESEARCH ARTICLE SUMMARY

MICROBIOLOGY

Trypanosome doublet microtubule structures reveal flagellum assembly and motility mechanisms

Xian Xia, Michelle M. Shimogawa, Hui Wang, Samuel Liu, Angeline Wijono, Gerasimos Langousis, Ahmad M. Kassem, James A. Wohlschlegel, Kent L. Hill*, Z. Hong Zhou*

INTRODUCTION: Parasitic trypanosomes, including *Trypanosoma brucei* and related species, cause severe disease in humans and other mammals. As excavates that diverged early within the eukaryotic lineage, trypanosomes also offer great opportunities for novel biological discovery. The single flagellum of *T. brucei* drives its motility and plays key roles in cell division, morphogenesis, and host interactions. Unlike most organisms, the trypanosome flagellum beats with a helical waveform that propagates tip to base. Central to flagellar motility is a conserved 9+2 axoneme, in which nine doublet microtubules (DMTs) surround a pair of singlet microtubules, with radial spokes (RSs) projecting inward from the DMTs to contact the central pair complex. Flagellar beating is powered by thousands of dynein motors arrayed between DMTs, with outer (ODA) and inner (IDA) dynein arms performing complementary roles and regulated by other axonemal complexes such as the nexin-dynein regulatory complex (N-DRC). An extra-axonemal filament unique to trypanosomes and other *Euglenozoa*, the paraflagellar rod (PFR), is attached alongside the axoneme, providing elastic resistance against axoneme bending.

RATIONALE: Recent cryo–electron microscopy (cryo-EM) studies have resolved high-resolution structures of DMTs from different organisms, revealing core features of flagellum assembly and motility and also identifying lineage-specific adaptations. Notably lacking in these analyses are members of the excavata clade, which includes trypanosomes and other devastating pathogens. This presents a critical knowledge gap in our understanding of pathogen biology and evolution of mechanisms for assembly and operation of one of the most iconic structures of eukaryote biology.

RESULTS: We determined the 96-nm repeat structure of split *T. brucei* DMTs with attached ODAs, IDAs, RSs, and N-DRC using high-resolution cryo-EM. A total of 154 different axonemal proteins were identified, including 40 proteins unique to the trypanosome lineage. Trypanosome DMTs are further distinguished from those of other organisms by incorporation of extra paralogs for several microtubule inner proteins (MIPs), inner junction filament proteins, and proteins outside the DMT. We identified all subunits of the trypanosome-specific ponticulus and proteins on the DMT outer surface that may form attachments to the PFR. Using in-depth structural analysis combined with direct interrogation through knockdown of target proteins, we have defined MIP assembly mechanisms and unique features of the trypanosome axoneme.

DMTs were unexpectedly captured in a curved state, bending approximately 3° per 96-nm repeat with the B-tubule on the concave side, with dyneins in a pre–power stroke configuration. This contrasts with prior cryo–electron tomography reconstructions of the *T. brucei* axoneme and all high-resolution structures of split DMTs from other organisms, in which DMTs are straight with dyneins in the post–power stroke configuration. Compared with the post–power stroke state, motor domains of ODAs and IDAs shift toward the microtubule minus end in the pre–power stroke structure. Structural changes in the ODA linker are transmitted through the tail, which pivots upward and forward around the docking site on the DMT. This movement of the tail and associated intermediate chain–light chain tower accommodates concomitant repositioning of the motor domains from the adjacent dynein in the array. These findings led us to propose a "dragon boat" model for dynein-dependent movement of adjacent DMTs in the flagellar axoneme.

CONCLUSION: Our work expands our fundamental understanding of what it takes to build and operate a motile axoneme and also identifies parasite-specific adaptations that present potential targets for therapeutic or transmission-blocking agents. Our studies indicate that mechanisms for bending axonemal DMTs were established at or near the time of the last eukaryotic common ancestor, with eukaryotic diversification accompanied by lineage-specific axonemal proteins that alter DMT properties. These evolutionary adaptations enable each organism and cell type to produce a flagellar waveform that meets the needs of its specific functions and environments. ■

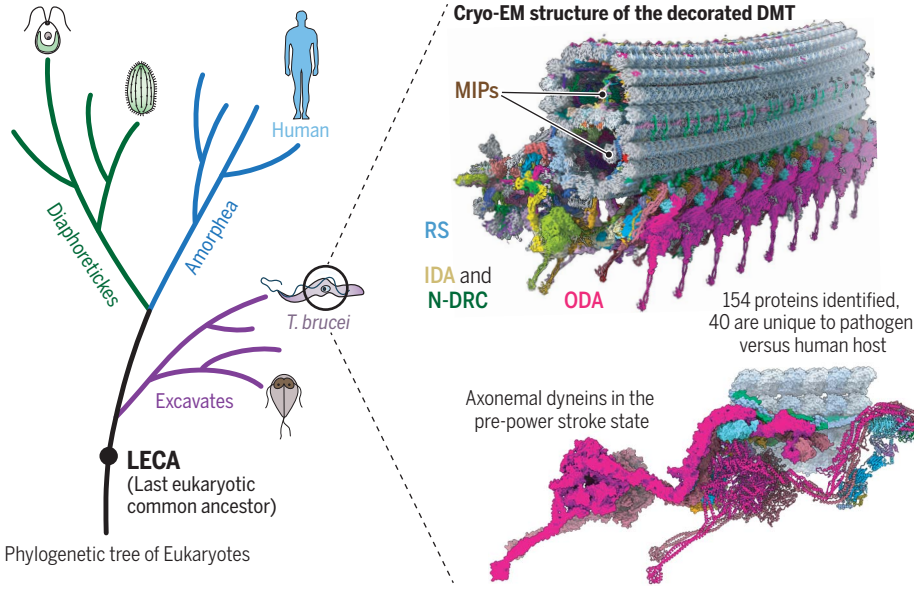

Cryo-EM structure of the decorated DMT from *T. brucei*. The phylogenetic tree of eukaryotes shows that the human parasite *T. brucei* diverged early within the eukaryotic lineage, before the emergence of separate lineages for humans and other organisms used as models for cilium biology. Magnified view of the *T. brucei* flagellum shows the cryo-EM structure of the *T. brucei* DMT with attached ODAs, IDAs, RSs, and N-DRC. Dyneins in the pre–power stroke state are docked to the curved DMT.

The list of author affiliations is available in the full article online.
*Corresponding author. Email: kenthill@microbio.ucla.edu (K.L.H.); hong.zhou@ucla.edu (Z.H.Z.)
Cite this article as X. Xia *et al.*, *Science* **387**, eadr3314 (2025).
DOI: 10.1126/science.adr3314

READ THE FULL ARTICLE AT
https://doi.org/10.1126/science.adr3314

RESEARCH ARTICLE

MICROBIOLOGY

Trypanosome doublet microtubule structures reveal flagellum assembly and motility mechanisms

Xian Xia[1,2], Michelle M. Shimogawa[1], Hui Wang[1,2,3], Samuel Liu[1,2], Angeline Wijono[1], Gerasimos Langousis[1], Ahmad M. Kassem[4], James A. Wohlschlegel[4], Kent L. Hill[1,2,5]*, Z. Hong Zhou[1,2]*

The flagellum of *Trypanosoma brucei* drives the parasite's characteristic screw-like motion and is essential for its replication, transmission, and pathogenesis. However, the molecular details of this process remain unclear. Here, we present high-resolution (up to 2.8 angstrom) cryo–electron microscopy structures of *T. brucei* flagellar doublet microtubules (DMTs). Integrated modeling identified 154 different axonemal proteins inside and outside the DMT and, together with genetic and proteomic interrogation, revealed conserved and trypanosome-specific foundations of flagellum assembly and motility. We captured axonemal dynein motors in their pre–power stroke state. Comparing atomic models between pre– and post–power strokes defined how dynein structural changes drive sliding of adjacent DMTs during flagellar beating. This study illuminates structural dynamics underlying flagellar motility and identifies pathogen-specific proteins to consider for therapeutic interventions targeting neglected diseases.

Trypanosomatid parasites, *Trypanosoma brucei*, *T. cruzi*, and *Leishmania* spp., are vector-borne pathogens of humans and livestock that cause substantial human suffering worldwide and limit economic development in some of the world's most impoverished regions (*1*). Trypanosomes diverged early within the eukaryotic lineage (*2*) and are a rich source of biological discovery (*3*). The parasite's flagellum plays a central role in parasite biology (*4*–*10*), transmission (*11*–*15*), and pathogenesis (*16*–*18*), and its multitude of critical functions make the flagellum an attractive drug target (*19*). The *Trypanosoma* genus was named for the organism's characteristic helical flagellar waveform that propagates tip to base, with the entire cell rotating around its long axis as it translocates with the flagellum tip leading (*20*, *21*). This form of motility is adaptive for movement through viscous environments (*22*) such as those encountered in the insect vector and mammalian host (*13*, *18*). The trypanosome flagellum is built on a canonical 9+2 axoneme with nine doublet microtubules (DMTs) surrounding a central pair complex (CPC) containing two singlet microtubules, with radial spokes (RSs) projecting inward from each DMT (*23*–*25*). Running alongside the axoneme and attached to DMTs 4 to 7 is the paraflagellar rod (PFR) (Fig. 1A), a lattice-like filament specific to trypanosomes and other *Euglenozoa* (*26*). Axoneme beating is driven by outer dynein arms (ODAs) and inner dynein arms (IDAs), with the nexin-dynein regulatory complex (N-DRC) and RSs providing regulatory functions (*4*, *6*, *27*–*31*). These proteins decorate the outer surface of each DMT and are organized into a 96-nm repeating unit (*32*).

Recent high-resolution cryo–electron microscopy (cryo-EM) structures of DMTs from several organisms have identified proteins binding the luminal face (microtubule inner proteins, MIPs) and external surface (microtubule outer proteins, MOPs) of DMTs to influence axoneme assembly, stability, and motility (*33*–*36*). An emerging model is that axoneme beating is driven by conserved dynein motors, whereas lineage-specific proteins contribute to differences in flagellar beating and motility between different organisms and cell types (*23*, *33*, *34*, *37*–*39*). Notably, however, a high-resolution DMT structure has not yet been reported for any of the kinetoplastids, an early branching clade that includes several pathogens (*2*). This represents a critical gap in knowledge of pathogen biology and the evolution of basic mechanisms of flagellar assembly and motility.

Axonemal dyneins are evolutionarily related to cytoplasmic dyneins, each composed of a heavy chain (HC) and accessory intermediate chains (ICs) and light chains (LCs) (*40*, *41*). HCs carry out the mechanochemical cycle and share a conserved domain architecture: a ring of six AAA+ ATPase domains, a microtubule-binding domain (MTBD) connected by a coiled-coil stalk to the AAA+ ring, and a linker domain that connects the AAA+ ring to the tail, which assembles with the intermediate chain–light chain (IC-LC) tower and connects to cargo (*40*, *41*). Axonemal dyneins permanently dock to the A-tubule of each DMT through the tail domain and reversibly bind the B-tubule of the adjacent DMT through the MTBD. Using the energy of ATP hydrolysis, dyneins cycle through a power stroke and recovery stroke in which structural rearrangements of the motor drive relative sliding of adjacent DMTs (*32*, *42*, *43*). Interdoublet connections through the N-DRC constrain movements between DMTs, causing them to bend (*42*, *44*–*46*). Propagation of DMT bending along the axoneme to generate flagellar beating requires spatiotemporal coordination of dynein activity through interconnections among dyneins, RSs, the N-DRC, and the CPC. Although recent work on cytoplasmic dynein has allowed comparison of high-resolution structures in the pre– versus post–power stroke states (*47*–*50*), all high-resolution structures of microtubule-bound axonemal dynein were in the post–power stroke state (*33*, *51*–*53*). Thus, although low-resolution cryogenic electron tomography (cryo-ET) provides a general description of the overall dynein cycle (*44*, *54*, *55*), details of the structural dynamics underlying dynein-powered flagellar beating are poorly defined.

Structure determination of the decorated 96-nm DMT repeat from *T. brucei*

We developed a workflow that includes mild protease digestion, sonication, and incubation with ATP to overcome the high stability of the axoneme-PFR superstructure and split the *T. brucei* axoneme into DMTs suitable for single-particle cryo-EM (fig. S1). A cryo-EM map with local resolutions up to 2.8 Å for the 48-nm DMT repeat was obtained using a focused refinement strategy (fig. S2, table S1, and materials and methods). For dyneins, RSs, and N-DRC, we used an integrated strategy of focused classification, center shift, particle subtraction, and focused refinement (fig. S3 and materials and methods). To obtain a full axonemal repeat map, individual maps of the 96-nm DMT repeat, including MIPs, MOPs, ODAs, IDAs, RSs, and N-DRC, were obtained separately and combined in silico (fig. S3). All DMT-associated structures observed in the published cryo-ET map of the intact axoneme (*23*) were well resolved in the cryo-EM map (Fig. 1B and Movie 1), indicating that the intact DMT structure was well preserved in our workflow.

To identify proteins from cryo-EM maps and to build an atomic model of the entire DMT, an integrative approach was used to incorporate information from de novo modeling, AlphaFold-based structure prediction (*56*, *57*), homolog modeling, and proteomic analysis (fig. S4 and materials and methods). In this way, an atomic model of the 96-nm axonemal repeat was generated, with only the RS3 head unmodeled

[1]Department of Microbiology, Immunology, and Molecular Genetics, University of California, Los Angeles, CA, USA. [2]California NanoSystems Institute, University of California, Los Angeles, CA, USA. [3]Department of Bioengineering, University of California, Los Angeles, CA, USA. [4]Department of Biological Chemistry, University of California, Los Angeles, CA, USA. [5]Molecular Biology Institute, University of California, Los Angeles, CA, USA.
*Corresponding author. Email: kenthill@microbio.ucla.edu (K.L.H.); hong.zhou@ucla.edu (Z.H.Z.)

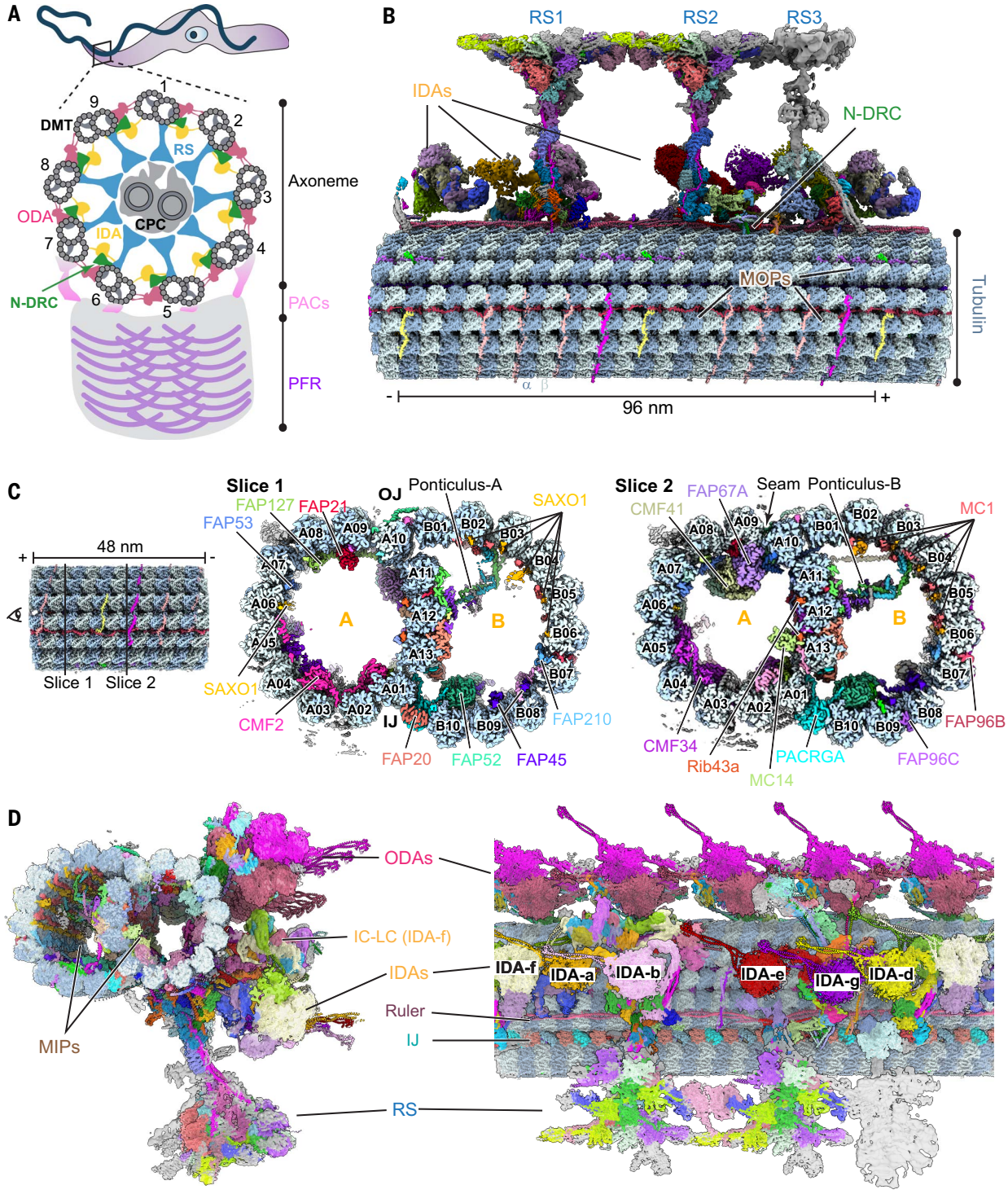

Fig. 1. Cryo-EM of the decorated 96-nm DMT repeat of *T. brucei*. (**A**) Diagrams showing the structure of the *T. brucei* cell and flagellum, including the DMT, ODA, IDA, RS, N-DRC, CPC, PFR, and PFR-axoneme connectors (PACs). (**B**) Cryo-EM map of the 96-nm repeat of the decorated DMT. (**C**) Two cross sections of the 48-nm repeat cryo-EM map showing densities for MIPs and MOPs. The IJ, OJ, and A-tubule seam are labeled. (**D**) Two orthogonal views showing the 96-nm cryo-EM map in superposition with the atomic model.

(figs. S5 to S8). In total, 154 different axonemal proteins were identified and modeled, showing the power of this AI-based integrative strategy (tables S2 and S3). Among these, 52 were MIPs located inside the DMT and 20 were MOPs bound directly to the outer surface of the DMT (Fig. 1C and movie S1). The model also contains 15 proteins that make up the two-headed ODA, 32 that comprise six different IDAs, 27 in the RSs, and 10 in the N-DRC (Fig. 1D and Movie 1). Trypanosomes are distinguished from other organisms by having extra paralogs of several conserved flagellar proteins (*58*), and the resolution of our cryo-EM map allowed us to distinguish these, demonstrating that they each

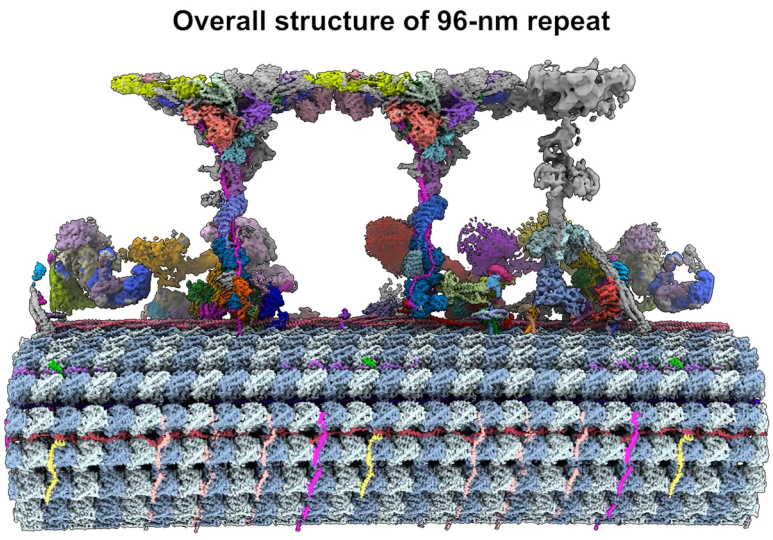

Movie 1. Cryo-EM map of the 96-nm repeat reconstruction of *T. brucei* DMTs. Overall structure of the decorated 96-nm repeat, including MIPs, MOPs, ODAs, IDAs, RSs, and the N-DRC. Identified proteins are colored as in Fig. 1; unassigned densities are in gray.

contribute to the DMT structure (fig. S5B and table S2). We also identified proteins that shared domain structure and axoneme position with flagellar proteins in other organisms but were not detectable previously by sequence homology (table S2). Of the 154 identified proteins, 40 are specific to *T. brucei* and the kinetoplastid lineage, contributing to the distinctive features of the trypanosome axoneme.

Structural comparison of DMTs from *T. brucei* and human (pathogen versus host)

T. brucei is a deadly pathogen that requires its flagellum for viability (*59*, *60*), host-parasite interaction (*5*, *9*, *12*), and the motility that drives pathogenesis and transmission (*14*, *16*). Therefore, it is informative to consider lineage-specific elaborations of the parasite axoneme relative to that of the human host (Fig. 2, A to C). Compared with the 34 MIPs currently identified in human respiratory cilia (*33*, *61*), there are a total of 52 MIPs in the *T. brucei* DMT, which are distributed between the A- and B-tubules. Approximately half of these are shared with humans, and the rest are lineage specific (Fig. 2, B and C). One particularly notable trypanosomatid-specific elaboration is the ponticulus, which transects the B-tubule and provides direct physical connections across the entire tubule (*23*, *62*–*64*). We identified all ponticulus subunits (discussed below) and showed that they are restricted to the trypanosomatid lineage (table S2). The *T. brucei* genome lacks the tektins that dominate the human A-tubule (*33*, *37*, *61*), as well as a few other A-tubule and B-tubule MIPs. Thus, our structure delineates several notable differences between the pathogen and its human host, presenting potential targets to consider for therapeutic interventions aimed at combating disease.

Paralogs and lineage-specific MIPs suggest expanded functionality and signaling capacity in the A-tubule

The *T. brucei* flagellum must meet organism-specific motility needs and interface with signaling pathways that regulate parasite motility (*11*, *12*, *65*). Our structure identifies lineage-specific MIPs in the protofilament (pf) ribbon region (pfsA11-12-13-01) (*66*, *67*) with the capacity to meet such needs (Fig. 2, D to E). For example, four Rib72 homologs, three copies of CMF2 and one each of CMF3, CMF4, and CMF34/CARP4, are spaced 8 nm apart within the 48-nm repeat. These correspond to six copies of a single Rib72 in *Chlamydomonas* (*36*) and three copies each of two Rib72 homologs in mammals and *Tetrahymena* (fig. S9, A and B) (*34*, *35*, *37*). RNA interference (RNAi) knockdown of individual *T. brucei* Rib72 paralogs affects motility differently, demonstrating that they are not functionally redundant (*58*). The C terminus of each paralog contains an EF-hand domain (*68*) (fig. S9, A and B, and movie S2), whereas the N terminus binds Rib43a/CARP9, which, like CMF34/CARP4, is a cAMP response protein (CARP) that functions in *T. brucei* cAMP signal transduction (*69*, *70*). Thus, expansion of the *T. brucei* Rib72 family may bridge Ca^{2+} and cAMP signaling with the motility apparatus.

The *T. brucei* A-tubule is further distinguished from that of most other organisms by having two paralogs for FAP161 (FAP161A and FAP161B) and the lineage-specific TbRib46. The latter protein runs 48 nm longitudinally between pfA01 and pfA13 (Fig. 2E) and contains four Mn motifs for microtubule binding and stabilization (*71*); thus it may accommodate the stability needs of the trypanosome axoneme (*23*). Trypanosome-specific ring MIP and ring-associated MIP (RAM) structures located at pfsA08-09 by cryo-ET (*23*) have been found to consist of five and three proteins, respectively (fig. S9C). Additional lineage-specific proteins (MC9, MC14, TbRib42, and TbRib26b) bind to Rib43a in the protofilament ribbon region (Fig. 2E).

Homologous A-tubule MIPs in *T. brucei* generally exhibit the same position and structure as counterparts in other organisms (*36*) (Fig. 2, D and E). It is noteworthy, however, that *T. brucei* FAP129 has no significant sequence homology to *Chlamydomonas* FAP129 but binds to FAP127 and protrudes through the microtubule wall at pfsA07-08 to contact the ODA docking complex (ODA-DC) (fig. S10) in a manner similar to *Chlamydomonas* FAP129 (*36*).

B-tubule MIPs and mechanism of inner junction filament assembly

Trypanosomes have more B-tubule MIPs than any other organism reported to date, including the core inner junction (IJ) MIPs FAP106 and FAP52, together with IJ filament subunits PACRG and FAP20 (Fig. 3A and table S2). The trypanosome IJ exhibits several unusual features, including proteins specific to trypanosomes and extra paralogs of conserved proteins. FAP106 is a critical interaction hub that links B-tubule MIPs on both sides of the IJ (*72*, *73*). In *Chlamydomonas* and mammals, three copies of FAP106 are positioned 16 nm apart within each 48-nm repeat (*35*, *36*). In *T. brucei*, however, there are only two copies of FAP106, "FAP106A," within each repeat, whereas the third iteration is replaced by a related protein, "FAP106B," thereby generating a pseudo–16-nm pattern within the 48-nm repeat (Fig. 3A and fig. S12A). Each FAP106A connects one copy of FAP45, located along pfsB07-08 or pfsB08-09, to a trypanosome-specific protein, MC5, on pfsA12-13 (Fig. 3, A, D, and F, and fig. S12A). Conversely, FAP106B connects FAP210, located on pfsB06-07, to a distinct trypanosome-specific protein, MC10, on pfA12 (Fig. 3, A, D, and E, and fig. S12A). Another trypanosome-specific protein, MC4, is arranged at 16-nm intervals along pfA12-13, where each copy binds to either MC5 or MC10 (Fig. 3A and fig. S12A). This arrangement provides a structural mechanism for differential placement of PACRG paralogs (*72*) and two mysterious holes within the IJ filament (fig. S12B), as described below.

T. brucei has two PACRG homologs, PACRGA and PACRGB (*74*), that are nonredundant and proposed to alternate with FAP20 in the IJ filament (*72*), as reported for *Tetrahymena* (*34*). Our structure confirms this organization by directly distinguishing the two paralogs (Fig. 3G) and establishes that each hole in the IJ filament (*23*) corresponds to a missing PACRGB. The PACRGB N terminus contacts MC5 (Fig. 3, A and C, and fig. S12A), whereas the PACRGA N terminus contacts MC4 and FAP52 (Fig. 3, A and B, and fig. S12A). This arrangement provides

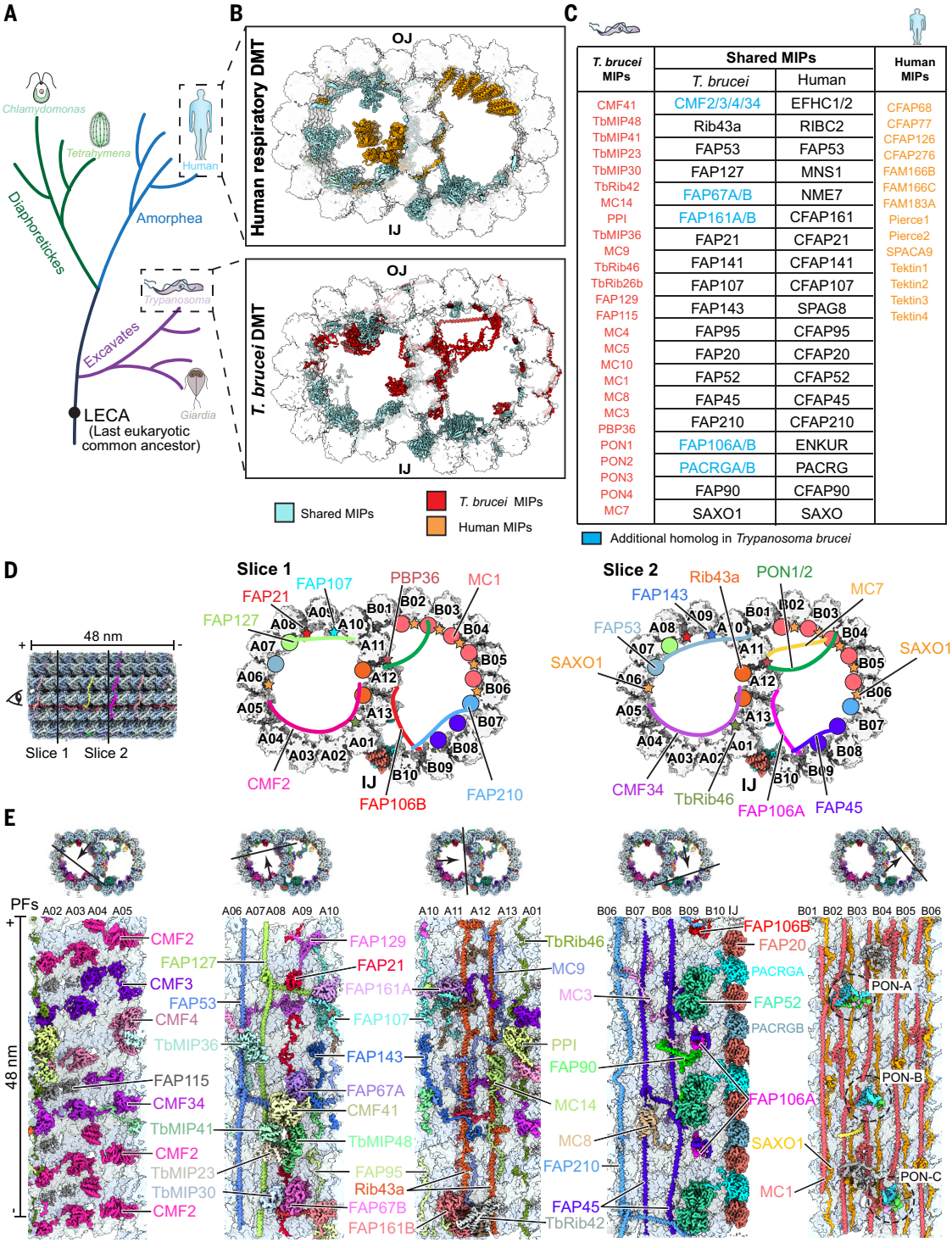

T. brucei MIPs	Shared MIPs		Human MIPs
	T. brucei	Human	
CMF41	CMF2/3/4/34	EFHC1/2	CFAP68
TbMIP48	Rib43a	RIBC2	CFAP77
TbMIP41	FAP53	FAP53	CFAP126
TbMIP23	FAP127	MNS1	CFAP276
TbMIP30	FAP67A/B	NME7	FAM166B
TbRib42	FAP161A/B	CFAP161	FAM166C
MC14	FAP21	CFAP21	FAM183A
PPI	FAP141	CFAP141	Pierce1
TbMIP36	FAP107	CFAP107	Pierce2
MC9	FAP143	SPAG8	SPACA9
TbRib46	FAP95	CFAP95	Tektin1
TbRib26b	FAP20	CFAP20	Tektin2
FAP129	FAP52	CFAP52	Tektin3
FAP115	FAP45	CFAP45	Tektin4
MC4	FAP210	CFAP210	
MC5	FAP106A/B	ENKUR	
MC10	PACRGA/B	PACRG	
MC1	FAP90	CFAP90	
MC8	SAXO1	SAXO	
MC3			
PBP36			
PON1			
PON2			
PON3			
PON4			
MC7			

Fig. 2. MIPs of *T. brucei* DMTs. (**A**) Phylogenetic tree of eukaryotes (*2*) showing that excavates branch early at the base of the tree. (**B**) Overall structural comparison between DMTs from *T. brucei* flagella and human respiratory cilia (PDB:8J07) (*33*), with MIPs colored by conservation. (**C**) Table of MIPs in *T. brucei* and human DMTs. (**D**) Cartoon representation of MIPs in a longitudinal and lateral network to stabilize the DMT. Tubulin protofilaments are shown in surface representation and labeled. MIPs are represented by cartoon shapes. (**E**) Longitudinal views of the DMT lumen from different angles, as indicated by black arrows. Conserved A-tubule MIPs include longitudinally oriented MIPs (Rib43a, FAP127, FAP53, and FAP21) and MIPs that extend laterally across several protofilaments (FAP141, FAP107, FAP143, FAP95, FAP129, and FAP115).

a mechanism for directing the placement of PACRGB by interaction with MC5 versus PACRGA by interaction with MC4 (Fig. 3G and fig. S12A) and explains the loss of PACRGB but not PACRGA when FAP106A is removed, because MC5 but not MC4 depends on FAP106A (*72*). MC10 lacks the PACRGB-binding domain found in MC5 (Fig. 3A and fig. S12A), explaining the holes in the *T. brucei* IJ filament (*23*) where MC10 substitutes for MC5 (holes 1 and 2 in Fig. 3G).

To further test our proposed mechanism for IJ assembly and to investigate the MIP interactions revealed by cryo-EM, we used RNAi to generate *FAP106A* (*72*) and *FAP106B* knockdown (KD) parasites (fig. S13, A and B). Quantitative proteomics of *FAP106B*-KD versus control flagella showed FAP106B and MC10 to be the only two proteins significantly reduced in the knockdown (fig. S13F and table S4), supporting our model (Fig. 3A and fig. S12B) and indicating that MC10 assembly depends on FAP106B. We next prepared split DMTs from *FAP106A*-KD and *FAP106B*-KD cells for single-particle cryo-EM (fig. S11, A and B). *FAP106A*-KD led to a loss of FAP106A, as well as MC3, MC5, MC8, FAP45, and FAP90, from the structure (fig. S12C), consistent

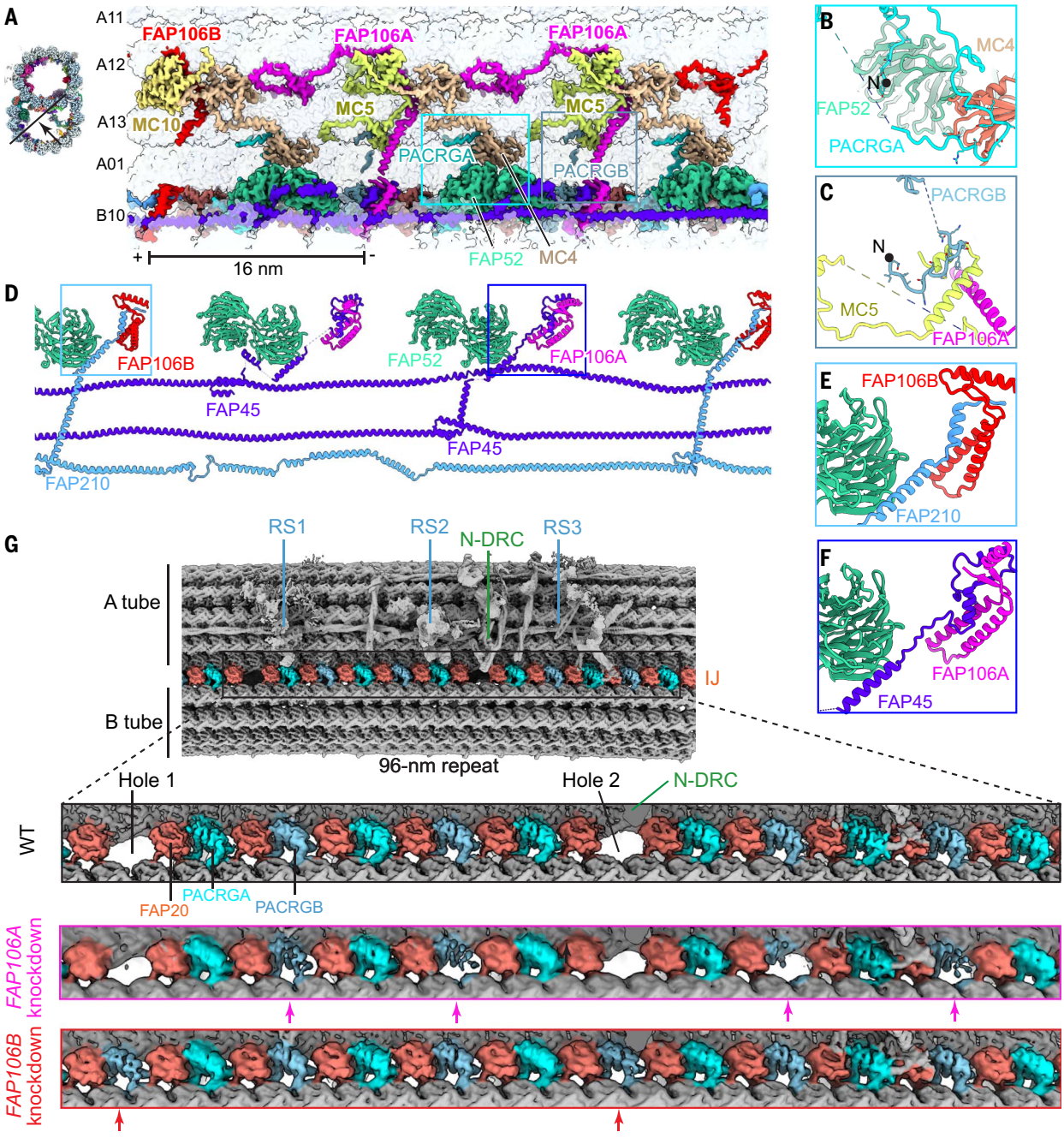

Fig. 3. The presence of FAP106B in the B-tubule leads to holes in the IJ filament. (**A**) MIPs in the B-tubule at the IJ region show a pseudo–16-nm repeat pattern. The viewing angle is indicated on the cross section in the left panel. (**B** and **C**) Interaction of the N-terminal tails of PACRGA with MC4 (B) and PACRGB with MC5 (C). Proteins are shown as ribbon diagrams. (**D** to **F**) Interactions at the IJ involving FAP106A, FAP106B, FAP52, FAP45, and FAP210. Proteins are shown as ribbon diagrams, with FAP106B and FAP106A regions enlarged in (E) and (F), respectively. (**G**) Longitudinal views of the 96-nm repeat from wild type (WT) and mutant DMTs showing the IJ filament. Positions of the two holes in WT are labeled. Arrows indicate the changes in the IJ filament upon FAP106A and FAP106B knockdown.

with prior proteomic and cryo-ET analysis (*72*). The occupancy of PACRGB decreased substantially in the *FAP106A*-KD structure, leading to four additional holes within the IJ filament in each 96-nm repeat (Fig. 3G). In the DMT structure from *FAP106B*-KD cells, FAP106B and MC10 are replaced by FAP106A and MC5, respectively (fig. S12D), indicating that FAP106B prevents the assembly of FAP106A at this location. In full support of our model for IJ filament assembly (fig. S12B) and confirming a key role for FAP106B, the IJ holes in the *FAP106B*-KD were filled by two additional PACRGB subunits within the 96-nm repeat with no impact on N-DRC subunits (Fig. 3G). Therefore, the locations of IJ holes in *T. brucei* are dictated by MIP placement rather than steric clash with the N-DRC as observed for *Chlamydomonas* and mammals (*33*, *38*). Flagellum length and propulsive motility of *FAP106B*-KD cells appear mostly normal (fig. S13, D and E), suggesting that replacement of FAP106B by FAP106A and loss of IJ holes do not have a substantial impact on propulsive cell motility, although we cannot rule out impacts on movement through the host or vector environment.

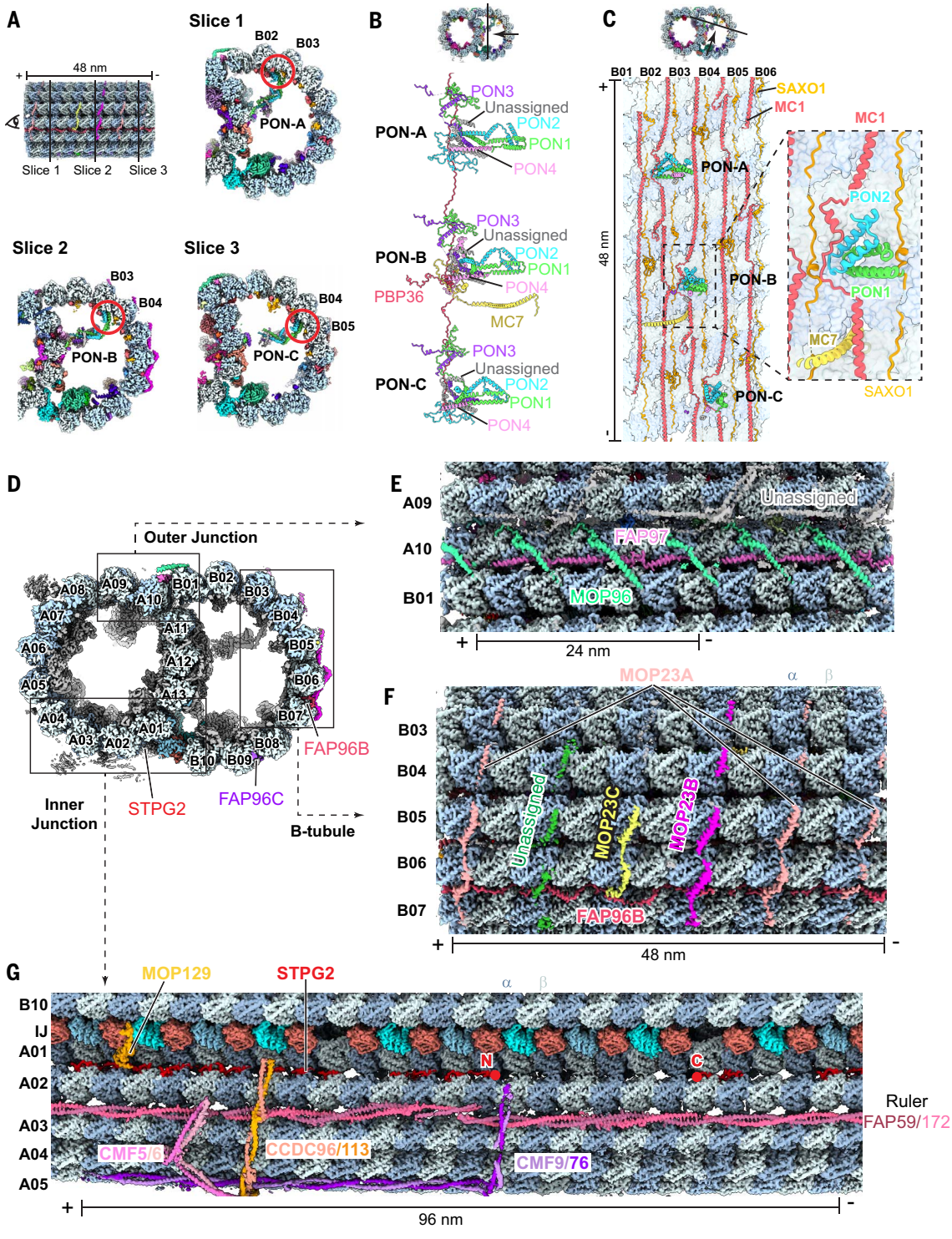

Fig. 4. Structures of the ponticulus and MOPs. (**A**) Three cross sections of the B-tubule from the 48-nm DMT repeat showing the positions of PON-A, PON-B, and PON-C. Red circles indicate the positions where ponticulus tips interact with B-tubule protofilaments. (**B**) Protein compositions of the three ponticuli. (**C**) Interactions of the ponticulus tips with the B-tubule. (**D**) Cross section of the 48-nm DMT repeat showing the filamentous proteins on the outer surface of the DMT. The MIPs are shown in gray. Boxed regions indicate the color-coded MOPs shown in (E) to (G). (**E** to **G**) MOPs at the OJ region (E), B-tubule surface (F), and the IJ region (G) have 24-, 48-, and 96-nm periodicities, respectively. Four pairs of filamentous proteins, FAP59/172, CMF9/76, CMF5/6, and CCDC96/113, bind in the grooves of protofilaments or on the outer surfaces of the A-tubule and function as binding platforms for other axonemal protein complexes such as RS, IDA, and the N-DRC.

Subunit composition of the ponticulus

The ponticulus ("little bridge") of trypanosomes transects the B-tubule and is arguably among the first MIP structures described in any species, having been reported six decades ago (*62*–*64*). There are three ponticulus structures in each 48-nm repeat spaced 16 nm apart (*23*). We designate these as PON-A, PON-B, and PON-C, starting from the distal end of the DMT (Fig. 4, A to C). Proteins PON1 to PON4 are shared by all three ponticuli, whereas MC7 is specific to PON-B (Fig. 4B and fig. S14B). Phylogenetic analysis indicates that these proteins are specific to trypanosomatids (table S2), consistent with the ponticulus structure having been observed exclusively in this lineage. At pfsA11-A13, the base of PON-A and PON-C present as nearly identical structures in which the N termini of subunits PON1, PON2, and PON3 attach directly to pfsA11-12 while also being stabilized through interaction with another trypanosome-specific protein, "ponticulus binding protein 36" (PBP36), which extends 48 nm along the interface between pfA11 and pfA12 (Fig. 4B and fig. S14B). The base of PON-B differs from that of PON-A and PON-C, because the location occupied by the PON2 N terminus is instead

occupied by an additional subunit, MC7, and a well-resolved PON4. The N and C termini of adjacent PBP36 overlap at the position where PON-B attaches to pfA12, with the C terminus wrapping around pfA12 to insert into the A-tubule. The N termini of ponticulus proteins are rich in zinc fingers, which enhance interactions among subunits (fig. S14A).

All three ponticuli transect the entire B-tubule lumen to bind different B-tubule protofilaments; PON-A, PON-B, and PON-C bind to pfB02, pfB03, and pfB04, respectively (Fig. 4, A and C). The interface of each ponticulus with B-tubule protofilaments is mediated by the C-terminal helix-turn-helix of PON1 and PON2 that inserts between α- and β-tubulin. PON1 and PON2 are further stabilized by interactions with three copies of the trypanosome-specific MC1 protein that run parallel to pfB02, pfB03, and pfB04 (Fig. 4C). Two additional copies of MC1 run parallel to pfB01 and pfB05, but do not interact with the ponticuli. A copy of SAXO1 runs parallel to each copy of MC1 (Fig. 4C). For PON-B, the C terminus of MC7 makes an additional interface with B-tubule protofilaments through a helix that inserts between pfB03 and pfB04 (Fig. 4C).

Ponticuli are observed in mature flagella but not in nascent flagella (*62*). With the ponticulus subunits identified, we examined their distribution using the TrypTag protein localization resource (fig. S15) (*75*, *76*). Individual ponticulus subunits did not show clear preferential distribution in mature versus nascent flagella (fig. S15). Our model indicates that PBP36 is important for stabilizing the ponticulus. To test this idea, we generated *PBP36* knockdown parasites (*PBP36*-KD) (fig. S13B) and determined their DMT composition (fig. S13F) and structure (fig. S11C). Quantitative proteomics showed no significant change in the abundance of ponticulus subunits in the knockdown (fig. S13F and table S5), but the ponticulus structure was poorly resolved (fig. S14B). Thus, ponticulus subunits remain in the axoneme but do not form a stable structure in the absence of PBP36, perhaps because of an incomplete attachment to the A-tubule. The ability to present as stable or flexible forms could provide an explanation for the paradoxical observation that ponticulus proteins are present in both mature and nascent flagella (fig. S15) (*75*) but are only stabilized into a structure visible by EM in mature flagella (*62*).

MOPs provide a linkage between the axoneme and PFR

A notable feature of the trypanosome DMT structure is an abundance of proteins on the outer surface of tubulin protofilaments, which is distinct from that of other organisms (fig. S16). We identified 20 such MOPs, seven of which are specific to trypanosomes (MOP96, MOP23A, MOP23B, MOP23C, MOP84A, MOP84B, and MOP129) (Fig. 4, D to G, and table S2).

Three longitudinal MOPs, STPG2, FAP96B, and FAP96C, are identified as "wedge" MOPs (*38*) inserted in grooves between protofilaments (Fig. 4, D, F, and G), where they interact with protofilaments through a PG-rich domain (*34*, *38*) or a distinct MTBD found in the CFAP96 protein family (*38*). Prior studies in *T. brucei* demonstrated that FAP96C depends on FAP106A for assembly (*72*), and our current data indicate that this reflects a FAP96C interaction with FAP90, which in turn interacts with FAP45 (fig. S12A), both of which are lost upon FAP106A knockdown (*72*). Our structural data also provide a mechanistic explanation for the "hemi-axoneme" phenotype observed two decades ago upon knockdown of CMF9 or CMF76 in *T. brucei* (*58*). CMF9/76 forms a filamentous dimer that provides an anchoring point on the A-tubule for the N-DRC and IDA-f (Fig. 4G), both of which provide important linkages between adjacent *T. brucei* DMTs (*23*, *31*). Our studies therefore provide a structural basis for prior functional observations regarding MIP and MOP interdependencies and axoneme assembly.

The most prominent lineage-specific structure in the trypanosome flagellum is the paraflagellar rod (PFR), a massive filament that runs along one side of the axoneme, connected to DMTs 4 to 7 (*77*, *78*). Prior studies identified "PFR-axoneme connectors" (PACs) specific to each of these DMTs (*77*), although the identity of the PAC subunits was not resolved. By fitting the DMT single-particle structure into a cryo-ET map of the whole *T. brucei* axoneme (fig. S17), we found lineage-specific MOPs that are at the axoneme-PFR interface and thus candidate PAC subunits. MOP96 connects pfsA10-B01, arcing diagonally over the outer junction (OJ) (Fig. 4E), which corresponds to one of the PAC attachment sites (fig. S17) (*77*). Likewise, MOP23A, MOP23B, and MOP23C are paralogous proteins spaced 8 nm apart and binding laterally across pfsB03-B07 (Fig. 4F). This region of the B-tubule also corresponds to one of the PAC attachment sites described previously (*77*). Although we do not identify DMT-specific structures (*23*), MOP96 and MOP23 densities are weak compared with other proteins, as would be anticipated if only present on a subset of DMTs, as is the case for PACs (*77*). Our structure studies thus offer insight into proteins at the axoneme interface with the PFR, a lineage-specific hallmark of the trypanosome flagellum that is essential for *T. brucei* motility (*79*).

Structure of ODAs in a pre–power stroke conformation

ODAs are the main force-generating motors for flagellar beating (*40*). Each 96-nm repeat contains four ODA complexes, docked in a head-to-tail arrangement on the A-tubule (Fig. 5A). *T. brucei* ODAs contain two HCs (ODA-α and ODA-β) (*23*, *80*) and we resolve both of these, as well as two intermediate chains (IC70 and IC78), seven light chains (LC7a/LC7b, LC6/LC8/LC10, and LC2/LC9), and four subunits of the ODA-DC (DC1/2, TbDC65, and TbDC13) (Fig. 5B and see below). Trypanosome-specific structural adaptations include two unassigned densities at the neck region of the HCs (fig. S19A) and an insertion within AAA6 of ODA-β that projects upward from the face of the AAA+ ring and would coincide with a site of connection to the PFR on DMTs 4 to 7 (fig. S19A) (*23*). We also did not observe a density at the position of LC4 in *Chlamydomonas* (*51*). Notwithstanding these differences, *T. brucei* ODA-α and ODA-β dimerize through interactions between their N-terminal tails and the IC-LC tower (Fig. 5B and fig. S19A) in an organization that is conserved with that of *Chlamydomonas* (*51*), *Tetrahymena* (*52*, *53*), and humans (*33*). Thus, the basic mechanisms for ODA-α/β assembly appear to have been established by the time of the last eukaryotic common ancestor.

ODA attachment to the DMT is mediated by tail interaction with a DC composed of a conserved coiled-coil dimer of DC1 and DC2 proteins, together with accessory proteins (*35*, *51*, *53*). In *T. brucei*, DCs in the proximal and distal regions of the axoneme are composed of distinct DC1 and DC2 proteins (*81*). We cannot distinguish proximal versus distal DC1/2 from our cryo-EM density, although the proximal proteins fit slightly better so are used in our model (materials and methods and table S3). The N-terminal half of the DC1/2 coiled-coil is embedded between pfA07 and pfA08, whereas the flexible C-terminal portion bends away from the DMT surface to interact with the ODA tail (Fig. 5, A and B). The structure reveals two lineage-specific components found only in trypanosomes, here called TbDC65 and TbDC13 (tables S2 and S3) to reflect their molecular weights, as well as an unidentified density that binds to TbDC13 (Fig. 5B and fig. S19C). TbDC65 and TbDC13 are located near the upward bend in the DC1/2 complex (fig. S19C), contacting the HC tail and IC78 of the neighboring ODA-α to facilitate the head-to-tail ODA arrangement (Fig. 5A) that is critical for flagellar beating (*52*). Recent functional analysis of the TbDC65 homolog in *Leishmania* indicates that it is ODA associated (*82*). In mammals and *Chlamydomonas*, head-to-tail ODA arrangement is also achieved through a combination of conserved proteins (DC1/2) and lineage-specific proteins (*35*, *51*), suggesting that DC1/2-docking is ancestral, whereas accessory proteins have evolved to accommodate organism-specific needs.

In contrast to prior cryo-ET reconstruction of the intact *T. brucei* axoneme, in which ODAs are in the post–power stroke configuration (fig. S18) (*23*), our atomic model shows that motor domains of both ODA-α and ODA-β are in a pre–power stroke state with linkers bent ~90° in the hinge region (*48*) to interact with AAA2/3 (Fig. 5, C and D) instead of interacting with

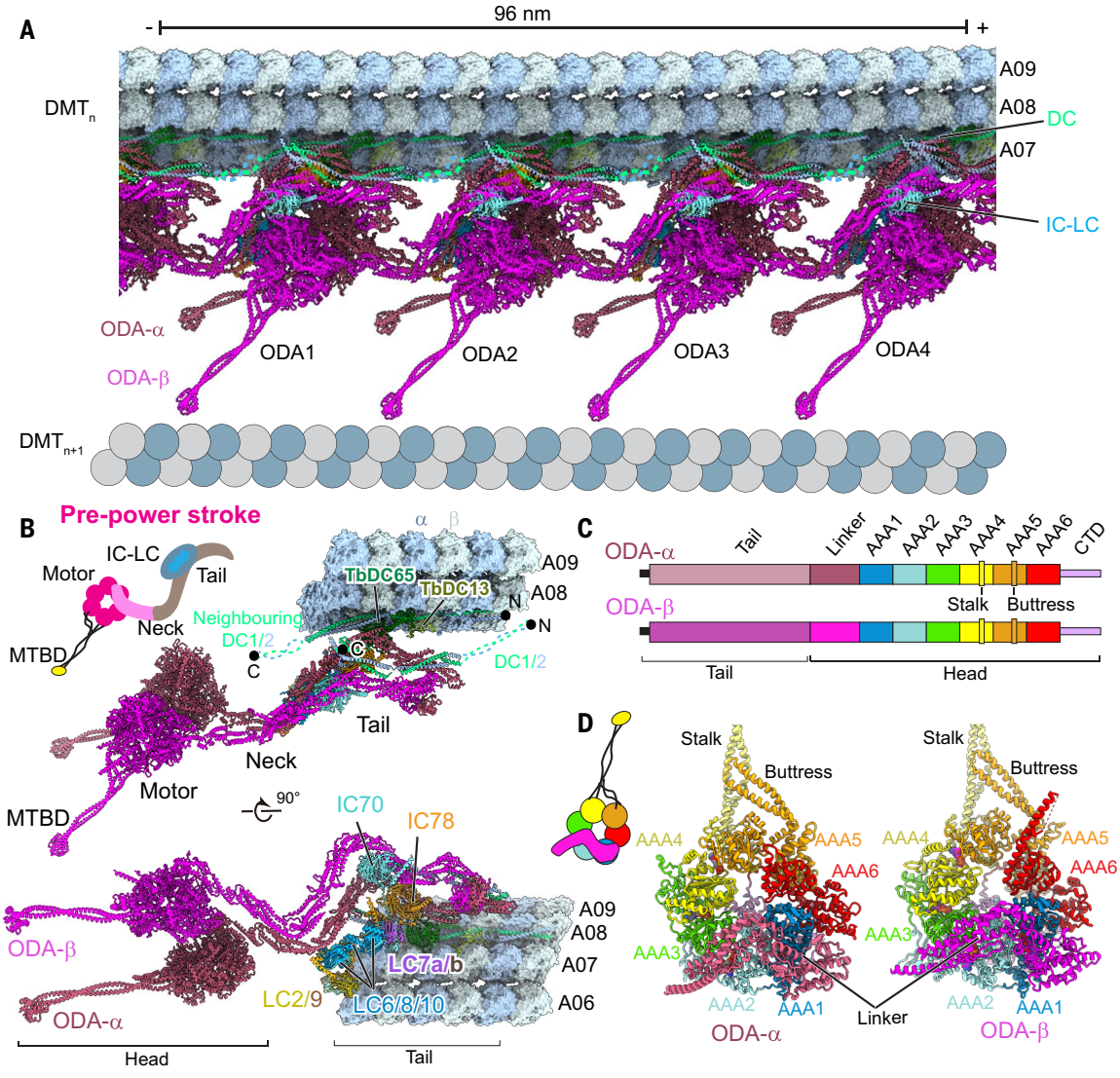

Fig. 5. Structure of the ODA in pre–power stroke state. (**A**) Structure of the ODA array attached to the DMT through the DC. ODA and DC are in ribbon representation, pfA06 to pfA09 from the ODA-docked DMT (DMT$_n$) are shown in surface representation. The relative position of the adjacent DMT (DMT$_{n+1}$), not resolved in the structure, is indicated by a cartoon of tubulin protofilaments. (**B**) Structure of one ODA unit attached to the DMT. The IC-LC tower consists of two intermediate chains (IC70 and IC78) and five homo- or heterodimers of light chains (LC7a/7b, LC8/LC10, LC8/LC8, LC6/LC8, and LC2/LC9). Dotted lines indicate the potential extended directions of DC1/2. (**C**) Sequence diagram showing domain organization of ODA-α and ODA-β. (**D**) Atomic models of ODA-α and ODA-β motor domains showing the pre–power stroke state of ODA, with cartoon representation as an inset for reference.

AAA4/5, as seen in the post–power stroke state (*49*–*52*). Although it is unclear why dyneins were captured in pre–power stroke, we found that, consistent with the pre–power stroke state, all four nucleotide binding sites (AAA1 to AAA4) in both HCs are occupied by nucleotides (fig. S19B). According to densities at the nucleotide-binding pockets, we tentatively assigned ATP (or ADP + Pi) and ADP at the binding pockets of AAA1 to AAA3 and AAA4, respectively.

ODA complexes are preassembled in the cytoplasm and transported to their site of incorporation into the axoneme (*83*, *84*), invoking the need for regulatory systems that prevent premature dynein activation. In *Tetrahymena*, the assembly factor Shulin locks the ODA complex in the pre–power stroke state, but inactive with MTBDs clustered (fig. S20A) (*85*). Although it remains to be determined whether trypanosomes use a Shulin complex, biochemical analysis supports cytoplasmic preassembly (*86*), and high conservation of ODA structure suggests conserved assembly mechanisms. Our high-resolution structure of natively docked, pre–power stroke ODA provides an opportunity to explore the conformational changes required for axoneme docking, because the pre–power stroke state represents the native state of most axonemal dyneins (*55*). Comparison of Shulin-locked (*85*) with DMT-docked ODA led us to propose that movements in motor and tail domains, primarily ODA-β, expose interfaces that allow direct interaction between the IC-LC tower and the IC70 β-propeller of one ODA complex and the motor domains of the adjacent ODA (figs. S19D and S20B). These interactions stabilize head-to-tail docking of adjacent ODA complexes, transforming them into an active configuration with ODA-α and ODA-β parallel to one another and free to undergo the mechanochemical cycle (fig. S20 and movie S3).

Structure and organization of IDAs on the DMT

The *T. brucei* genome encodes seven different dynein HCs that make up the double-headed IDA-f and five single-headed IDAs (IDA-a, IDA-b, IDA-e, IDA-g, and IDA-d), and each of these is

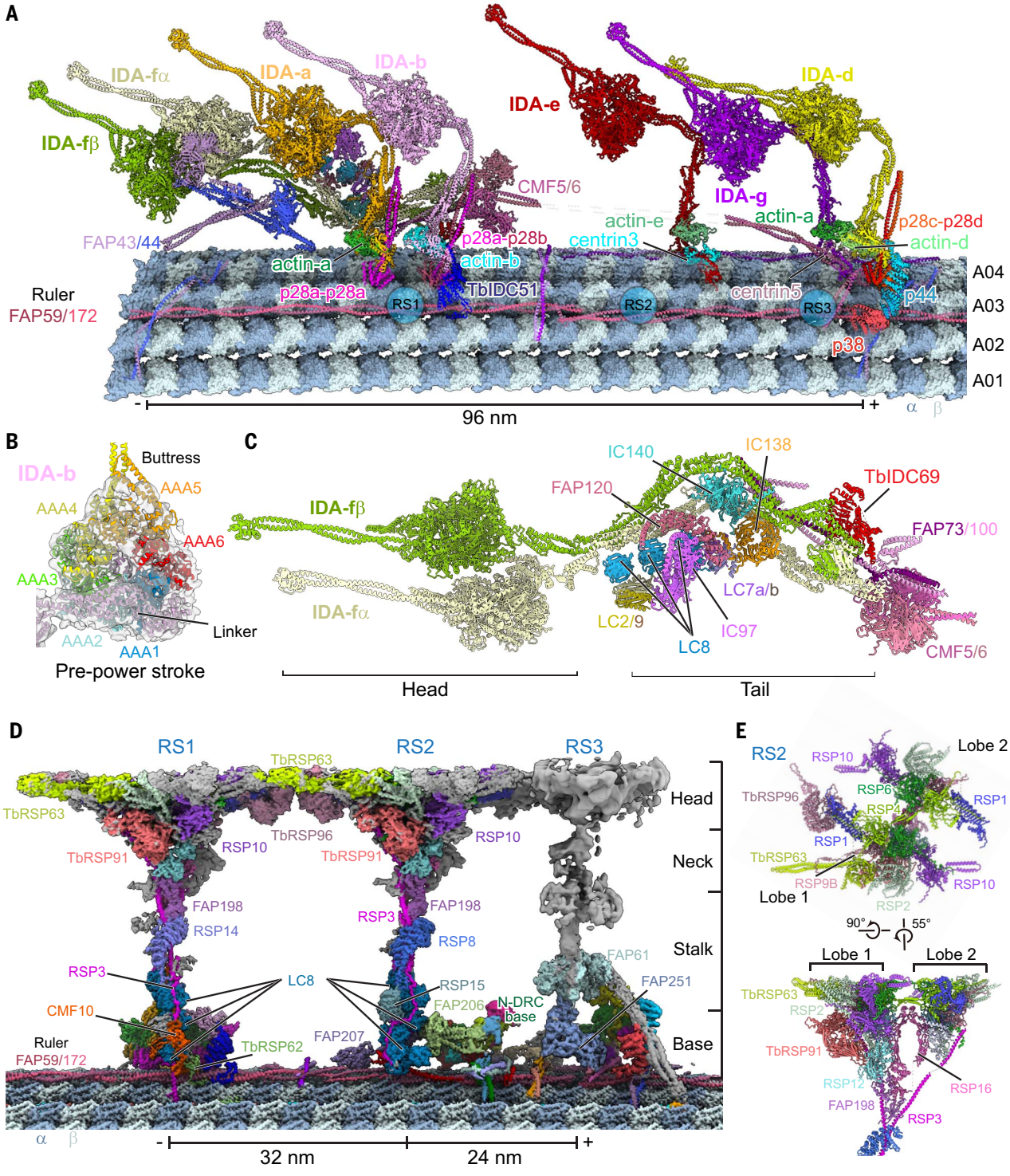

Fig. 6. Structures of the DMT-docked IDAs and RSs. (**A**) Atomic models of the double-headed IDA-f and five single-headed IDAs (IDA-a, IDA-b, IDA-e, IDA-g, and IDA-d) attached to the DMT. Tubulin pfA01 to pfA05 are shown in surface representation. Each IDA is docked on the DMT through different proteins. (**B**) Superposition of the atomic model with the cryo-EM map of the IDA-b motor domain showing the pre–power stroke state of IDA. (**C**) Atomic model of the double-headed IDA-f and associated docking proteins, ICs, and LCs. (**D**) Cryo-EM map of the DMT-attached radial spokes. (**E**) Two orthogonal views of the atomic model of the RS2 head.

identified according to cryo-EM densities of their structurally distinct HC tails (Fig. 6A and figs. S21 and S22). IDA-f contains two HCs (IDA-fα and IDA-fβ), several ICs, LCs, and docking proteins (FAP73/100, FAP43/44 and CMF5/6) (Fig. 6C and fig. S21) in an organization shared with *Chlamydomonas* (*33*). Consistent with their contribution to IDA-f function, depletion of CMF5, CMF6, or FAP43 in *T. brucei* causes severe motility defects (*58*, *87*). A lineage-specific protein, TbIDC69 (fig. S21), connects FAP73/100 to pfA05, enhancing the multipoint anchoring of IDA-f in *T. brucei*.

Compared with six single-headed IDAs in humans and *Chlamydomonas* (*33*), only five

were observed in the *T. brucei* cryo-EM structure, consistent with prior cryo-ET studies (*23*, *25*). Five different dynein HCs were unambiguously identified and assigned to IDA-a, IDA-b, IDA-e, IDA-g, and IDA-d, with IDA-c missing (Fig. 6A and fig. S22, A to C). Although IDA AAA+ motor domains were not as well resolved as ODAs, structural features clearly show that they are in the pre–power stroke state (Fig. 6B). Although *T. brucei* IDAs mostly share composition and structure with those of other organisms (*28*, *33*) (Fig. 6A and fig. S22), a lineage-specific protein, TbIDC51, aids in IDA-b docking to the DMT (Fig. 6A and fig. S22A), and a helix-turn-helix structure within DRC9 provides a lineage-specific connection to IDA-e (fig. S22B). *T. brucei* IDAs are further distinguished by having four different actin isoforms, four p28 isoforms, and two centrin isoforms (fig. S22, D and E), whereas human and *Chlamydomonas* IDAs have only a single isoform of each (*28*, *33*). Gene-specific knockdowns demonstrate nonredundant function for paralogous *T. brucei* IDA subunits (*88*, *89*), supporting the view that these represent adaptations that contribute to the organism's specific motility needs.

Structure of radial spokes

The *T. brucei* 96-nm repeat has three RSs (Fig. 6D) (*23*, *25*), similar to humans and different from *Chlamydomonas* (*27*, *28*, *33*). The head plus neck regions of *T. brucei* RS1 and RS2 are almost identical to one another (Fig. 6D). Although they include most proteins and interactions observed in the simpler spoke heads of *Chlamydomonas* and humans (*27*, *28*, *33*), they additionally contain three lineage-specific proteins (TbRSP63, TbRSP91, and TbRSP96) and two lineage-specific, unidentified densities on lobe 1 (Fig. 6D and fig. S23). These trypanosome adaptations expand the RS1-RS2 interface and enlarge lobe 1 to give it a "rotated K" appearance (fig. S23A) that, unlike lobe 1 in other organisms, is not symmetric with lobe 2 (Fig. 6E and fig. S23A). Instead of RS1 and RS2 contact through RSP1 as in other organisms (*28*), an expanded RS1-RS2 interface is mediated by lineage-specific TbRSP96 on RS1-lobe 2 directly contacting TbRSP96 and TbRSP63 on RS2-lobe 1 (figs. S23 and S24A). These contacts enlarge the highly acidic spoke head interface with the CPC projections (fig. S24B), potentially explaining why the CPC in *T. brucei* does not rotate relative to the spokes (*6*). The RS3 head and RS2-RS3 interface differ substantially from that of RS1-RS2, but molecular details remain unidentified (fig. S24A).

Conservation of RS docking to the A-tubule through adapter proteins that connect to the FAP59/172 ruler complex (fig. S25) (*27*, *28*, *33*) indicates that these systems arose early in evolution. One *T. brucei* innovation is replacement of FAP207 in RS1 with a lineage-specific protein, TbRSP62, connecting the RS1 base to tubulin (fig. S25A). Another *T. brucei* innovation is that FAP207 on RS2 has acquired an inactive kinesin motor domain that stabilizes RS2 attachment by binding to microtubules at a site made available by the absence of IDA-c (fig. S26). RS2 docking is further supported by the conserved FAP206 protein (fig. S25B), which was not observed in earlier RS cryo-EM structures (*28*, *33*), although functional studies indicate that it is required for RS2 and IDA-c docking in *Chlamydomonas* (*90*). We observed FAP206 connecting the RS2 base to the N-DRC, explaining the FAP206 mutant phenotype (*90*), and providing a conduit for regulatory signals from N-DRC to RS2.

N-DRC and IDA-f play central roles as interaction hubs

N-DRC and IDA-f interconnect ODAs, IDAs, and RSs, providing regulatory hubs for spatiotemporal coordination of dynein motors that is necessary for effective flagellar beating (fig. S27A) (*31*, *33*). The *T. brucei* N-DRC cryo-EM structure (fig. S27B) shares features with that of *Chlamydomonas*, *Tetrahymena*, and humans (*33*, *91*) and is consistent with the cryo-ET structure of intact *T. brucei* axonemes (*23*). Protein assignments for DRC1 to DRC5, DRC9 to DRC11, and trypanin are supported by biochemistry and functional analysis directly in *T. brucei* (*58*, *59*, *92*, *93*) (fig. S28). DRC3 sits at the bifurcation of the N-DRC linker and interacts with both IDA-e and IDA-g (fig. S27C), whereas a lineage-specific helix-turn-helix structure within DRC9 provides additional lineage-specific N-DRC-IDA connectivity (fig. S27D).

Our IDA-f model shows contacts conserved with *Chlamydomonas* (*33*) and additionally identifies molecular details of IDA-IDA interactions (fig. S27, A and E). The IDA-f complex connects directly with IDA-d and IDA-a. In turn, IDA-a connects with IDA-b, whereas IDA-d and IDA-g interconnect with each other, and IDA-g interacts directly with the N-DRC and IDA-e (fig. S27E). Thus, our studies reveal more extensive interconnections within the axoneme than observed in prior studies of post–power stroke configurations (*33*). Given the extensive conservation among the proteins involved, we propose that this enhanced connectivity reflects differences between pre– versus post–power stroke configurations throughout the axonemal 96-nm repeat, in addition to some lineage-specific differences.

Structural rearrangement of the axoneme between the post– and pre–power stroke states

Prior high-resolution studies of dynein natively docked to the DMT captured only the post–power stroke (*33*, *51*–*53*). Our findings thus provide an opportunity to define changes between post– and pre–power stroke states by comparing the atomic model for the pre–power stroke DMT (Fig. 7B) with the post–power stroke DMT atomic model from *Chlamydomonas* (*33*) and the post–power stroke cryo-ET structure

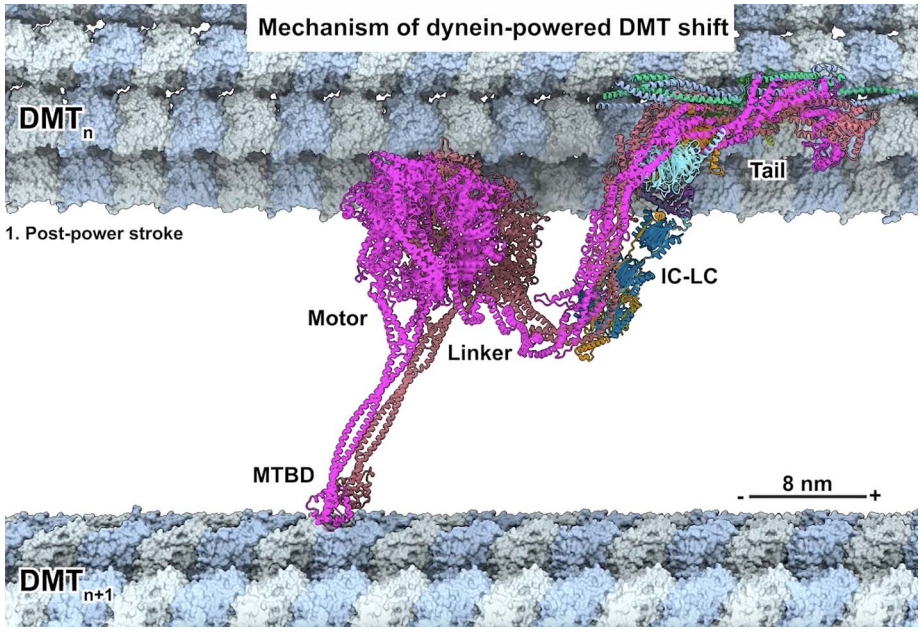

Movie 2. Mechanism of dynein-powered sliding between adjacent DMTs. Conformational changes in the recovery stroke and power stroke shown in Fig. 7D are presented. Only one ODA unit in the array is shown. Position of the adjacent DMT (DMT$_{n+1}$) was determined according to the cryo-ET map of *T. brucei* axoneme in the post–power stroke state (EMD-20013) (*23*). Model of the DMT$_{n+1}$-attached ODA in pre–power stroke was generated with the guidance of a cryo-ET map (EMD-5758) (*43*).

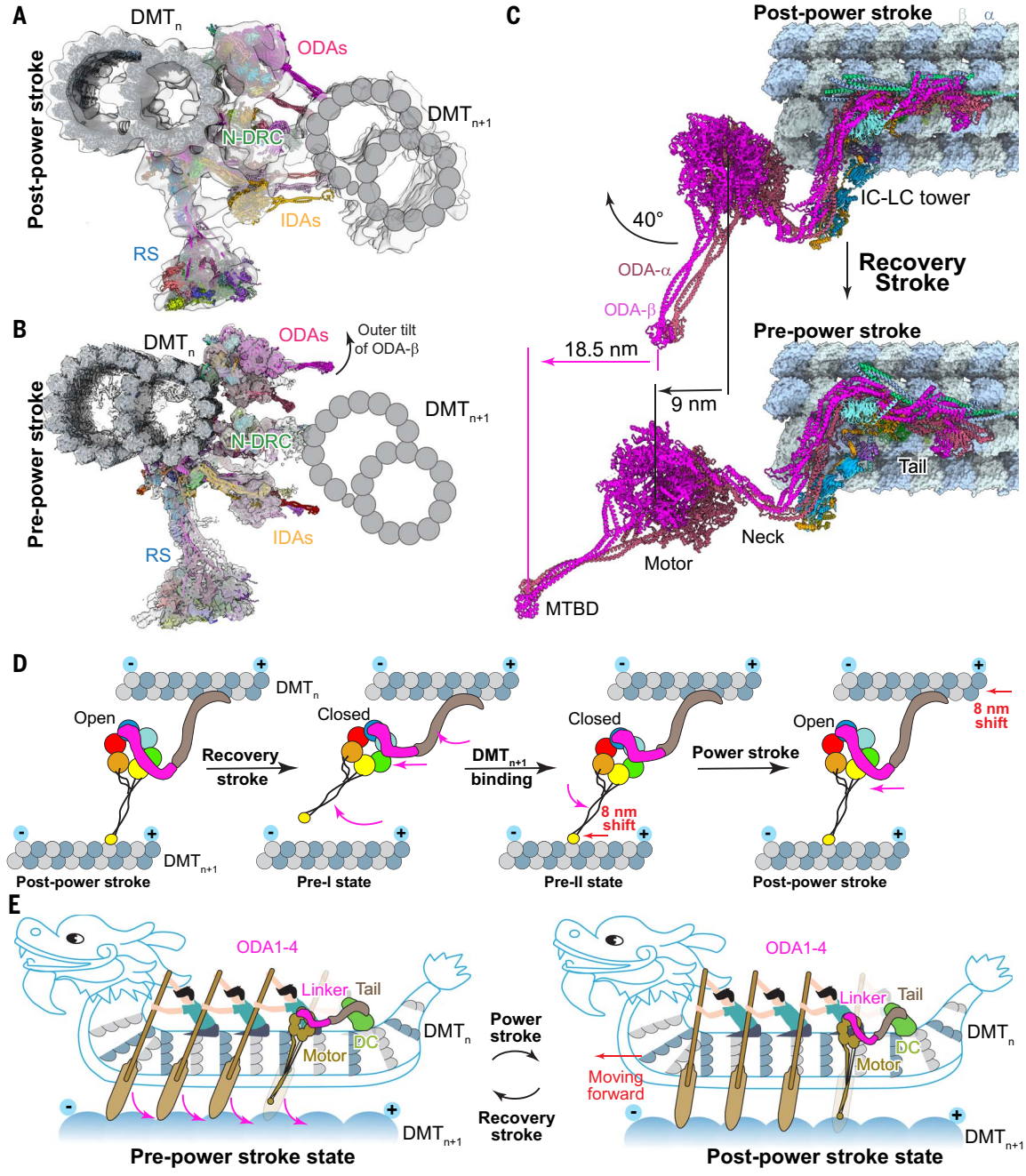

Fig. 7. Conformational changes of ODA during the ATP cycle. (**A**) Superposition of atomic model and cryo-ET map (EMD-20013) (*23*) of *T. brucei* 96-nm DMT repeat in the post–power stroke state. The MTBDs of dyneins bind to the adjacent DMT (DMT$_{n+1}$). A cartoon diagram of the adjacent DMT is placed on top of the map. (**B**) Superposition of atomic model and cryo-EM map of the 96-nm repeat in the pre–power stroke state. The position of the adjacent DMT is kept the same as that in the post–power stroke state. The MTBDs of dyneins are away from the adjacent DMT; the outer tilt of the ODA-β motor domain is indicated by a black arrow. (**C**) Conformational changes of ODA from post– to pre–power stroke state. Arrows indicate the movement of motor domains. (**D** and **E**) "Dragon boat" model of dynein-powered shift between adjacent DMTs. Conformational changes of ODA during the ATP cycle are shown by four representative cartoon schematics (D) from the post–power stroke state, pre-I state, pre-II state, to post–power stroke state with the DMT shifting 8 nm toward the microtubule minus end. The mechanism of dynein-powered sliding between adjacent DMTs resembles the movement of a dragon boat (E). The paddle represents the motor, and the arm and body of a crew member represent the linker and tail of the dynein, respectively.

of the intact axoneme from *T. brucei* (Fig. 7A and fig. S29) (*23*). In all structures, dynein motors are tandemly arrayed and natively docked to the DMT A-tubule, i.e., the cargo, whereas the cryo-ET structure gives the position of the adjacent DMT, i.e., the track. Structural comparison shows conformational changes in ODAs, IDAs, and N-DRC (Fig. 7C and figs. S30 and S31), thereby defining atomic-scale rearrangements not just within the motor but also among the interconnected network of axonemal complexes that cooperate to convert the dynein mechanochemical cycle into coordinated flagellar beating.

Going from post– to pre–power stroke, dynein heads of both ODA-α and ODA-β are shifted

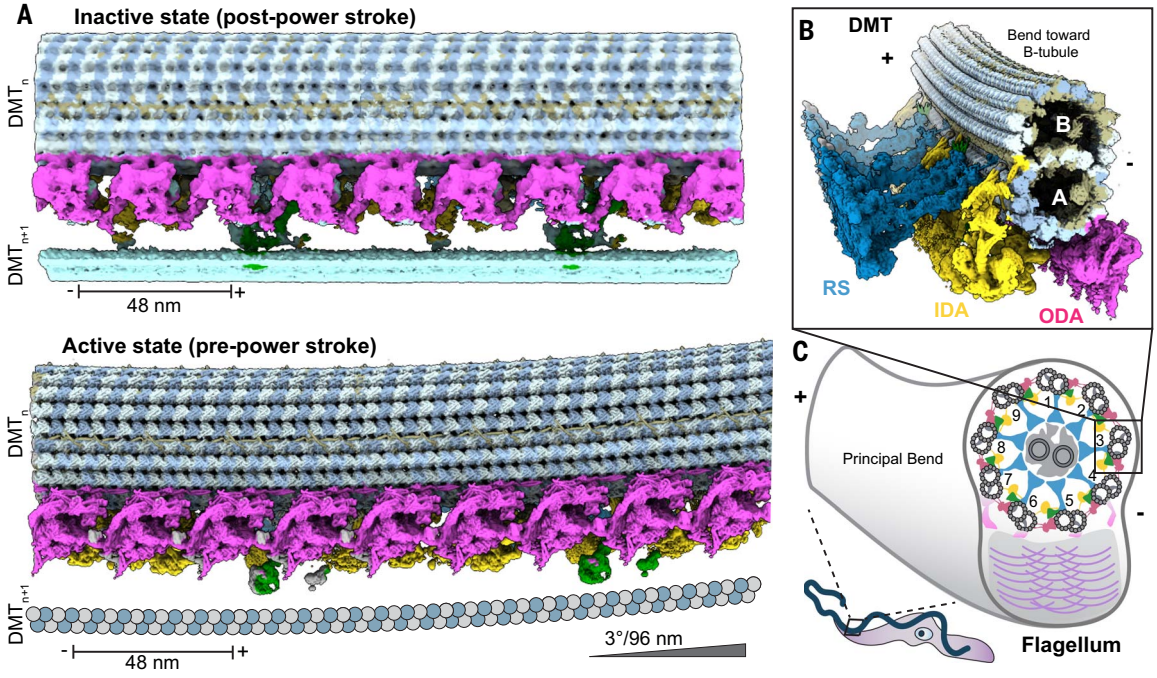

Fig. 8. Bent DMT of the pre–power stroke. (**A**) Structures of straight DMT with post–power stroke state dyneins (EMD-20013) (*23*) and curved DMT with pre–power stroke dyneins. The maps were generated by aligning two 96-nm repeats according to their overlapping regions. The anticipated position of the adjacent DMT (DMT_{n+1}) in the pre–power stroke state is indicated by a cartoon of tubulin protofilaments. (**B**) Cryo-EM map of the 192-nm DMT showing the bending of the DMT. (**C**) Cartoon diagram of the bent DMT in context of the *T. brucei* flagellum. The box indicates the DMT with a bend toward the B-tubule.

toward the minus end of the microtubule track by ~9 nm (Fig. 7C). This translocation is associated with several structural changes in the AAA+ rings and linkers, as well as substantial changes in the dynein tails and associated IC-LC tower. Changes in the AAA+ ring are similar to those described for recombinant cytoplasmic dynein (*41*, *48*, *50*). There is also a slight rotation of the ring (~40°), combined with a pivot near the site of AAA1 attachment to the linker (Fig. 7C). ODA-β tilts out of the plane of the DMT track, whereas ODA-α does not (Fig. 7B), indicating different roles for the two ODA motors. Structural changes of the AAA+ ring are coupled to bending in the linker hinge helix, as seen in cytoplasmic dynein (*48*) (fig. S30 and movie S4). Previously unidentified rearrangements within the linker (fig. S30D and Movie 2) straighten and lengthen linker subdomains 0 to 2, further expanding the distance between the motor head and tail. Linker structural changes are transmitted through the tail, which pivots around the docking site on the DMT, causing an upward and forward movement of the tail and IC-LC tower (Fig. 7C and Movie 2). The flexible region of DC1/2 allows pivoting of the tail at its docking site, whereas tail movements accommodate concomitant repositioning of the AAA+ ring from the adjacent dynein, which now contacts the tail and IC-LC tower. These combined movements define the recovery stroke that prepares ODA-α and ODA-β for subsequently carrying out the power stroke while accommodating coordinated movement of adjacent dyneins.

In our model of the recovery stroke, MTBDs of ODA-α and ODA-β move ~20 and ~18.5 nm, respectively, toward the microtubule minus end (Fig. 7C) with the MTBDs detached from the adjacent DMT (Fig. 7B), presumably representing the pre-I state (*44*). In preparation for the power stroke, this pre-I state converts to a pre-II state in which dynein heads are tilted ~20° back and MTBDs reattach to the adjacent DMT (*44*). Although we did not capture the pre-II state in our sample, the 8-nm step size of axonemal dynein (*94*) is smaller than the ~20-nm movement of MTBDs predicted in our model, consistent with backward movement of MTBDs from pre-I to pre-II (*44*). During the power stroke, ATP hydrolysis and product release drive structural rearrangements of the motor to drive cargo movement. Different models have been proposed for cytoplasmic dynein (*40*, *48*, *95*) and axonemal dynein (*44*), focusing either on bending of the linker in the hinge region or rotation of the AAA+ ring as the primary rearrangement that underlies cargo movement during the power stroke. Our studies support a combination of these two models, showing both bending at the linker hinge and rotation of the AAA+ ring (Fig. 7D) while also revealing structural changes within the linker and tail/IC-LC tower that contribute to moving cargo forward (Fig. 7, C and D, and Movie 2). Our combined studies lead us to propose a "dragon boat" model for dynein-dependent movement of adjacent DMTs in the flagellar axoneme (Fig. 7, D and E, and Movie 2).

In our pre–power stroke cryo-EM structure, the DMT was curved, bending ~3° per 96-nm repeat with the B-tubule on the concave side (Fig. 8). Within our cryo-EM dataset, no other conformations were observed, indicating that this curved DMT is predominant in our sample. By contrast, the published cryo-ET structure of *T. brucei* axonemes (*23*), and all structures of split DMTs from other species published to date (*33*, *51*, *53*), exhibit a straight DMT, with dyneins in the post–power stroke state. It is unclear whether the curved versus straight DMT reflects trypanosome-specific features of the split DMT or perhaps relates to the pre– versus post–power stroke state of the dyneins. Notably, however, replacement of ATP with ADP in the split DMT preparation resulted in DMTs with a variety of bending directions, in contrast to the constrained bending seen in the presence of ATP (fig. S32). The combined results suggest that increased length between the dynein tail and head in the pre– versus post–power stroke state causes the DMT to curve toward the side opposite dynein docking, although further work is needed to test this. Our discovery of an inherently curved state for isolated DMTs will now need to be considered in models to explain structural foundations of flagellar beating.

Conclusions

Excavates represent the root of the eukaryotic tree of life (*2*) and include many medically and economically significant pathogens, yet they have been notably underrepresented in structural studies of the axoneme. Here, we present the cryo-EM structure of the entire 96-nm DMT repeat of the *T. brucei* axoneme with resolution up to 2.8 Å, leading to atomic models for the decorated DMT, including MIPs, MOPs, ODAs, IDAs, RSs, and the N-DRC. We determined the identity, structure, location, and

interaction partners for 154 axonemal proteins in situ, revealing features foundational to eukaryotic flagellar motility, while also uncovering 40 proteins, predominantly MIPs and MOPs, that are found only in the pathogen and not the host. Moreover, we captured ODAs and IDAs in their pre–power stroke state, which, together with those in the post–power stroke state derived above for the same organism, allows direct comparisons to provide a comprehensive picture of dynein movement on the DMT track with cargo attached. Our findings provide a molecular blueprint for one of the most iconic and important structures of the trypanosome cell, defining trypanosome-specific proteins and expanding our fundamental understanding of what it takes to build a motile axoneme and how axonemal dyneins work together to drive flagellar beating.

Methods summary

Full details of the materials and methods are presented in the supplementary materials. Briefly, procyclic *T. brucei brucei* (strain 29-13) cultured in Cunningham's synthetic medium (SM) supplemented with fetal bovine serum were used for cryo-EM study. Demembranated flagella were prepared using detergent extraction and microtubule depolymerization, followed by protease treatment, sonication, and ATP incubation to split the flagella into individual DMTs for cryo-EM (fig. S1). Cryo-EM grids were generated by plunge-freezing the samples, and data collection was performed using a Titan Krios microscope, yielding 106,694 movies for wild type and additional datasets for the mutants. Structural determinations of 48- and 96-nm DMT repeats are summarized in table S1 and figs. S2 and S3. Atomic models were built using cryo-EM maps in combination with de novo modeling, AI-based predictions, homolog comparisons, and mass spectrometry data (fig. S4). The final 96-nm repeat model identified a total of 154 different axonemal proteins, including MIPs, MOPs, ODAs, IDAs, RSs, and the N-DRC (tables S2 and S3 and figs. S5 to S8). Structural-guided functional assays were conducted to support the cryo-EM studies, which included tetracycline-inducible knockdown of FAP106B and PBP36. These assays incorporated quantitative proteomics, growth curve analyses, motility analyses, fluorescence microscopy, and flagellum length measurements to characterize the effects of FAP106B and PBP36 knockdowns.

REFERENCES AND NOTES

1. M. Jamabo, M. Mahlalela, A. L. Edkins, A. Boshoff, Tackling sleeping sickness: Current and promising therapeutics and treatment strategies. *Int. J. Mol. Sci.* **24**, 12529 (2023). doi: 10.3390/ijms241512529; pmid: 37569903
2. C. Al Jewari, S. L. Baldauf, An excavate root for the eukaryote tree of life. *Sci. Adv.* **9**, eade4973 (2023). doi: 10.1126/sciadv.ade4973; pmid: 37115919
3. J. E. Donelson, M. J. Gardner, N. M. El-Sayed, More surprises from Kinetoplastida. *Proc. Natl. Acad. Sci. U.S.A.* **96**, 2579–2581 (1999). doi: 10.1073/pnas.96.6.2579 pmid: 10077550
4. G. Langousis, K. L. Hill, Motility and more: The flagellum of *Trypanosoma brucei*. *Nat. Rev. Microbiol.* **12**, 505–518 (2014). doi: 10.1038/nrmicro3274; pmid: 24931043
5. D. Salmon *et al*., Adenylate cyclases of *Trypanosoma brucei* inhibit the innate immune response of the host. *Science* **337**, 463–466 (2012). doi: 10.1126/science.1222753; pmid: 22700656
6. K. S. Ralston, A. G. Lerner, D. R. Diener, K. L. Hill, Flagellar motility contributes to cytokinesis in *Trypanosoma brucei* and is modulated by an evolutionarily conserved dynein regulatory system. *Eukaryot. Cell* **5**, 696–711 (2006). doi: 10.1128/EC.5.4.696-711.2006; pmid: 16607017
7. C. Branche *et al*., Conserved and specific functions of axoneme components in trypanosome motility. *J. Cell Sci.* **119**, 3443–3455 (2006). doi: 10.1242/jcs.03078; pmid: 16882690
8. F. F. Moreira-Leite, T. Sherwin, L. Kohl, K. Gull, A trypanosome structure involved in transmitting cytoplasmic information during cell division. *Science* **294**, 610–612 (2001). doi: 10.1126/science.1063775; pmid: 11641501
9. K. Vickerman, Developmental cycles and biology of pathogenic trypanosomes. *Br. Med. Bull.* **41**, 105–114 (1985). doi: 10.1093/oxfordjournals.bmb.a072036; pmid: 3928017
10. L. Tetley, K. Vickerman, Differentiation in *Trypanosoma brucei*: Host-parasite cell junctions and their persistence during acquisition of the variable antigen coat. *J. Cell Sci.* **74**, 1–19 (1985). doi: 10.1242/jcs.74.1.1; pmid: 4030903
11. S. Bachmaier *et al*., A multi-adenylate cyclase regulator at the flagellar tip controls African trypanosome transmission. *Nat. Commun.* **13**, 5445 (2022). doi: 10.1038/s41467-022-33108-z; pmid: 36114198
12. S. Shaw *et al*., Flagellar cAMP signaling controls trypanosome progression through host tissues. *Nat. Commun.* **10**, 803 (2019). doi: 10.1038/s41467-019-08696-y; pmid: 30778051
13. S. Schuster *et al*., Developmental adaptations of trypanosome motility to the tsetse fly host environments unravel a multifaceted in vivo microswimmer system. *eLife* **6**, e27656 (2017). doi: 10.7554/eLife.27656; pmid: 28807106
14. B. Rotureau, C. P. Ooi, D. Huet, S. Perrot, P. Bastin, Forward motility is essential for trypanosome infection in the tsetse fly. *Cell. Microbiol.* **16**, 425–433 (2014). doi: 10.1111/cmi.12230; pmid: 24134537
15. M. Oberholzer, M. A. Lopez, B. T. McLelland, K. L. Hill, Social motility in african trypanosomes. *PLOS Pathog.* **6**, e1000739 (2010). doi: 10.1371/journal.ppat.1000739; pmid: 20126443
16. M. M. Shimogawa *et al*., Parasite motility is critical for virulence of African trypanosomes. *Sci. Rep.* **8**, 9122 (2018). doi: 10.1038/s41598-018-27228-0; pmid: 29904094
17. T. Krüger, S. Schuster, M. Engstler, Beyond Blood: African Trypanosomes on the Move. *Trends Parasitol.* **34**, 1056–1067 (2018). doi: 10.1016/j.pt.2018.08.002; pmid: 30181072
18. J. L. Bargul *et al*., Species-Specific Adaptations of Trypanosome Morphology and Motility to the Mammalian Host. *PLOS Pathog.* **12**, e1005448 (2016). doi: 10.1371/journal.ppat.1005448; pmid: 26871910
19. J. Sáez Conde, S. Dean, Structure, function and druggability of the African trypanosome flagellum. *J. Cell. Physiol.* **237**, 2654–2667 (2022). doi: 10.1002/jcp.30778; pmid: 35616248
20. P. J. Walker, Organization of function in trypanosome flagella. *Nature* **189**, 1017–1018 (1961). doi: 10.1038/1891017a0; pmid: 13782746
21. A. Gruby, *Recherches et observations sur une nouvelle espèce d'hématozoaire, Trypanosoma sanguinis* (Comptes rendus hebdomadaire des séances de l'Académie des Sciences, 1843).
22. T. L. Jahn, E. C. Bovee, D. Weinman, M. Ristie, Protoplamic movements within cells. *Physiol. Rev.* **49**, 793–862 (1969). doi: 10.1152/physrev.1969.49.4.793; pmid: 4241846
23. S. Imhof *et al*., Cryo electron tomography with volta phase plate reveals novel structural foundations of the 96-nm axonemal repeat in the pathogen *Trypanosoma brucei*. *eLife* **8**, e52058 (2019). doi: 10.7554/eLife.52058; pmid: 31710293
24. T. Ishikawa, Axoneme structure from motile cilia. *Cold Spring Harb. Perspect. Biol.* **9**, a028076 (2017). doi: 10.1101/cshperspect.a028076; pmid: 27601632
25. L. C. Hughes, K. S. Ralston, K. L. Hill, Z. H. Zhou, Three-dimensional structure of the Trypanosome flagellum suggests that the paraflagellar rod functions as a biomechanical spring. *PLOS ONE* **7**, e25700 (2012). doi: 10.1371/journal.pone.0025700; pmid: 22235240
26. N. Portman, K. Gull, The paraflagellar rod of kinetoplastid parasites: From structure to components and function. *Int. J. Parasitol.* **40**, 135–148 (2010). doi: 10.1016/j.ijpara.2009.10.005; pmid: 19879876
27. X. Meng *et al*., Multi-scale structures of the mammalian radial spoke and divergence of axonemal complexes in ependymal cilia. *Nat. Commun.* **15**, 362 (2024). doi: 10.1038/s41467-023-44577-1; pmid: 38191553
28. M. Gui *et al*., Structures of radial spokes and associated complexes important for ciliary motility. *Nat. Struct. Mol. Biol.* **28**, 29–37 (2021). doi: 10.1038/s41594-020-00530-0; pmid: 33318703
29. X. Zhu, Y. Liu, P. Yang, Radial spokes - A snapshot of the motility regulation, assembly, and evolution of cilia and flagella. *Cold Spring Harb. Perspect. Biol.* **9**, a028126 (2017). doi: 10.1101/cshperspect.a028126; pmid: 27940518
30. A. L. Springer *et al*., Silencing of a putative inner arm dynein heavy chain results in flagellar immotility in *Trypanosoma brucei*. *Mol. Biochem. Parasitol.* **175**, 68–75 (2011). doi: 10.1016/j.molbiopara.2010.09.005; pmid: 20888370
31. T. Heuser, M. Raytchev, J. Krell, M. E. Porter, D. Nicastro, The dynein regulatory complex is the nexin link and a major regulatory node in cilia and flagella. *J. Cell Biol.* **187**, 921–933 (2009). doi: 10.1083/jcb.200908067; pmid: 20008568
32. R. Viswanadha, W. S. Sale, M. E. Porter, Ciliary motility: Regulation of axonemal dynein motors. *Cold Spring Harb. Perspect. Biol.* **9**, a018325 (2017). doi: 10.1101/cshperspect.a018325; pmid: 28765157
33. T. Walton *et al*., Axonemal structures reveal mechanoregulatory and disease mechanisms. *Nature* **618**, 625–633 (2023). doi: 10.1038/s41586-023-06140-2; pmid: 37258679
34. S. Kubo *et al*., Native doublet microtubules from Tetrahymena thermophila reveal the importance of outer junction proteins. *Nat. Commun.* **14**, 2168 (2023). doi: 10.1038/s41467-023-37868-0; pmid: 37061538
35. M. Gui *et al*., De novo identification of mammalian ciliary motility proteins using cryo-EM. *Cell* **184**, 5791–5806.e19 (2021). doi: 10.1016/j.cell.2021.10.007; pmid: 34715025
36. M. Ma *et al*., Structure of the decorated ciliary doublet microtubule. *Cell* **179**, 909–922.e12 (2019). doi: 10.1016/j.cell.2019.09.030; pmid: 31668805
37. L. Zhou *et al*., Structures of sperm flagellar doublet microtubules expand the genetic spectrum of male infertility. *Cell* **186**, 2897–2910.e19 (2023). doi: 10.1016/j.cell.2023.05.009; pmid: 37295417
38. M. R. Leung *et al*., Structural specializations of the sperm tail. *Cell* **186**, 2880–2896.e17 (2023). doi: 10.1016/j.cell.2023.05.026; pmid: 37327785
39. Z. Chen *et al*., De novo protein identification in mammalian sperm using in situ cryoelectron tomography and AlphaFold2 docking. *Cell* **186**, 5041–5053.e19 (2023). doi: 10.1016/j.cell.2023.09.017; pmid: 37865089
40. J. T. Canty, R. Tan, E. Kusakci, J. Fernandes, A. Yildiz, Structure and Mechanics of Dynein Motors. *Annu. Rev. Biophys.* **50**, 549–574 (2021). doi: 10.1146/annurev-biophys-111020-101511; pmid: 33957056
41. A. J. Roberts, T. Kon, P. J. Knight, K. Sutoh, S. A. Burgess, Functions and mechanics of dynein motor proteins. *Nat. Rev. Mol. Cell Biol.* **14**, 713–726 (2013). doi: 10.1038/nrm3667; pmid: 24064538
42. S. M. King, Turning dyneins off bends cilia. *Cytoskeleton* **75**, 372–381 (2018). doi: 10.1002/cm.21483; pmid: 30176122
43. T. J. Mitchison, H. M. Mitchison, Cell biology: How cilia beat. *Nature* **463**, 308–309 (2010). doi: 10.1038/463308a; pmid: 20090745
44. J. Lin, K. Okada, M. Raytchev, M. C. Smith, D. Nicastro, Structural mechanism of the dynein power stroke. *Nat. Cell Biol.* **16**, 479–485 (2014). doi: 10.1038/ncb2939; pmid: 24727830
45. P. Satir, How cilia move. *Sci. Am.* **231**, 44–52 (1974). pmid: 4439001
46. K. E. Summers, I. R. Gibbons, Adenosine triphosphate-induced sliding of tubules in trypsin-treated flagella of sea-urchin sperm. *Proc. Natl. Acad. Sci. U.S.A.* **68**, 3092–3096 (1971). doi: 10.1073/pnas.68.12.3092; pmid: 5289252
47. P. Chai *et al*., Cryo-EM reveals the mechanochemical cycle of reactive full-length human Dynein-1. bioRxiv, 2024.2005.2001.592044 (2024).
48. H. Schmidt, R. Zalyte, L. Urnavicius, A. P. Carter, Structure of human cytoplasmic dynein-2 primed for its power stroke. *Nature* **518**, 435–438 (2015). doi: 10.1038/nature14023; pmid: 25470043
49. T. Kon *et al*., The 2.8 Å crystal structure of the dynein motor domain. *Nature* **484**, 345–350 (2012). doi: 10.1038/nature10955; pmid: 22398446

50. A. P. Carter, C. Cho, L. Jin, R. D. Vale, Crystal structure of the dynein motor domain. *Science* **331**, 1159–1165 (2011). doi: 10.1126/science.1202393; pmid: 21330489
51. T. Walton, H. Wu, A. Brown, Structure of a microtubule-bound axonemal dynein. *Nat. Commun.* **12**, 477 (2021). doi: 10.1038/s41467-020-20735-7; pmid: 33473120
52. Q. Rao *et al*., Structures of outer-arm dynein array on microtubule doublet reveal a motor coordination mechanism. *Nat. Struct. Mol. Biol.* **28**, 799–810 (2021). doi: 10.1038/s41594-021-00656-9; pmid: 34556869
53. S. Kubo *et al*., Remodeling and activation mechanisms of outer arm dyneins revealed by cryo-EM. *EMBO Rep.* **22**, e52911 (2021). doi: 10.15252/embr.202152911; pmid: 34338432
54. N. Zimmermann, A. Noga, J. M. Obbineni, T. Ishikawa, ATP-induced conformational change of axonemal outer dynein arms revealed by cryo-electron tomography. *EMBO J.* **42**, e112466 (2023). doi: 10.15252/embj.2022112466; pmid: 37051721
55. J. Lin, D. Nicastro, Asymmetric distribution and spatial switching of dynein activity generates ciliary motility. *Science* **360**, eaar1968 (2018). doi: 10.1126/science.aar1968; pmid: 29700238
56. J. Abramson *et al*., Accurate structure prediction of biomolecular interactions with AlphaFold 3. *Nature* **630**, 493–500 (2024). doi: 10.1038/s41586-024-07487-w; pmid: 38718835
57. J. Jumper *et al*., Highly accurate protein structure prediction with AlphaFold. *Nature* **596**, 583–589 (2021). doi: 10.1038/s41586-021-03819-2; pmid: 34265844
58. D. M. Baron, K. S. Ralston, Z. P. Kabututu, K. L. Hill, Functional genomics in *Trypanosoma brucei* identifies evolutionarily conserved components of motile flagella. *J. Cell Sci.* **120**, 478–491 (2007). doi: 10.1242/jcs.03352; pmid: 17227795
59. K. S. Ralston, K. L. Hill, Trypanin, a component of the flagellar Dynein regulatory complex, is essential in bloodstream form African trypanosomes. *PLOS Pathog.* **2**, e101 (2006). doi: 10.1371/journal.ppat.0020101; pmid: 17009870
60. R. Broadhead *et al*., Flagellar motility is required for the viability of the bloodstream trypanosome. *Nature* **440**, 224–227 (2006). doi: 10.1038/nature04541; pmid: 16525475
61. M. Gui *et al*., SPACA9 is a lumenal protein of human ciliary singlet and doublet microtubules. *Proc. Natl. Acad. Sci. U.S.A.* **119**, e2207605119 (2022). doi: 10.1073/pnas.2207605119; pmid: 36191189
62. S. Vaughan, M. Shaw, K. Gull, A post-assembly structural modification to the lumen of flagellar microtubule doublets. *Curr. Biol.* **16**, R449–R450 (2006). doi: 10.1016/j.cub.2006.05.041; pmid: 16781996
63. K. Vickerman, The fine structure of Trypanosoma congolense in its bloodstream phase. *J. Protozool.* **16**, 54–69 (1969). doi: 10.1111/j.1550-7408.1969.tb02233.x; pmid: 4896668
64. W. Anderson, R. Ellis, Ultrastructure of Trypanosoma lewisi: Flagellum, microtubules, and the kinetoplast. *J. Protozool.* **12**, 483–499 (1965). doi: 10.1111/j.1550-7408.1965.tb03247.x
65. P. Surgue, M. R. Hirons, J. U. Adam, M. E. Holwill, Flagellar wave reversal in the kinetoplastid flagellate *Crithidia oncopelti*. *Biol. Cell* **63**, 127–131 (1988). doi: 10.1016/0248-4900(88)90051-2; pmid: 3203154
66. R. Linck *et al*., Insights into the structure and function of ciliary and flagellar doublet microtubules: Tektins, Ca2+-binding proteins, and stable protofilaments. *J. Biol. Chem.* **289**, 17427–17444 (2014). doi: 10.1074/jbc.M114.568949; pmid: 24794867
67. R. W. Linck, G. L. Langevin, Structure and chemical composition of insoluble filamentous components of sperm flagellar microtubules. *J. Cell Sci.* **58**, 1–22 (1982). doi: 10.1242/jcs.58.1.1; pmid: 7183681
68. A. Lewit-Bentley, S. Réty, EF-hand calcium-binding proteins. *Curr. Opin. Struct. Biol.* **10**, 637–643 (2000). doi: 10.1016/S0959-440X(00)00142-1; pmid: 11114499
69. S. Bachmaier *et al*., Novel kinetoplastid-specific cAMP binding proteins identified by RNAi screening for cAMP resistance in *Trypanosoma brucei*. *Front. Cell. Infect. Microbiol.* **13**, 1204707 (2023). doi: 10.3389/fcimb.2023.1204707; pmid: 37475965
70. M. K. Gould *et al*., Cyclic AMP effectors in African trypanosomes revealed by genome-scale RNA interference library screening for resistance to the phosphodiesterase inhibitor CpdA. *Antimicrob. Agents Chemother.* **57**, 4882–4893 (2013). doi: 10.1128/AAC.00508-13; pmid: 23877697
71. C. Bosc *et al*., Identification of novel bifunctional calmodulin-binding and microtubule-stabilizing motifs in STOP proteins. *J. Biol. Chem.* **276**, 30904–30913 (2001). doi: 10.1074/jbc.M011614200; pmid: 11413126
72. M. M. Shimogawa *et al*., FAP106 is an interaction hub for assembling microtubule inner proteins at the cilium inner junction. *Nat. Commun.* **14**, 5225 (2023). doi: 10.1038/s41467-023-40230-z; pmid: 37633952
73. A. A. Z. Khalifa *et al*., The inner junction complex of the cilia is an interaction hub that involves tubulin post-translational modifications. *eLife* **9**, e52760 (2020). doi: 10.7554/eLife.52760; pmid: 31951202
74. H. R. Dawe, H. Farr, N. Portman, M. K. Shaw, K. Gull, The Parkin co-regulated gene product, PACRG, is an evolutionarily conserved axonemal protein that functions in outer-doublet microtubule morphogenesis. *J. Cell Sci.* **118**, 5421–5430 (2005). doi: 10.1242/jcs.02659; pmid: 16278296
75. K. Billington *et al*., Genome-wide subcellular protein map for the flagellate parasite *Trypanosoma brucei*. *Nat. Microbiol.* **8**, 533–547 (2023). doi: 10.1038/s41564-022-01295-6; pmid: 36804636
76. S. Dean, J. D. Sunter, R. J. Wheeler, TrypTag.org: A Trypanosome Genome-wide Protein Localisation Resource. *Trends Parasitol.* **33**, 80–82 (2017). doi: 10.1016/j.pt.2016.10.009; pmid: 27863903
77. J. Zhang *et al*., Structure of the trypanosome paraflagellar rod and insights into non-planar motility of eukaryotic cells. *Cell Discov.* **7**, 51 (2021). doi: 10.1038/s41421-021-00281-2; pmid: 34257277
78. A. Y. Koyfman *et al*., Structure of *Trypanosoma brucei* flagellum accounts for its bihelical motion. *Proc. Natl. Acad. Sci. U.S.A.* **108**, 11105–11108 (2011). doi: 10.1073/pnas.1103634108; pmid: 21690369
79. P. Bastin, T. Sherwin, K. Gull, Paraflagellar rod is vital for trypanosome motility. *Nature* **391**, 548 (1998). doi: 10.1038/35300; pmid: 9468133
80. B. Wickstead, K. Gull, Dyneins across eukaryotes: A comparative genomic analysis. *Traffic* **8**, 1708–1721 (2007). doi: 10.1111/j.1600-0854.2007.00646.x; pmid: 17897317
81. B. F. L. Edwards *et al*., Direction of flagellum beat propagation is controlled by proximal/distal outer dynein arm asymmetry. *Proc. Natl. Acad. Sci. U.S.A.* **115**, E7341–E7350 (2018). doi: 10.1073/pnas.1805827115; pmid: 30030284
82. C. Fortz, B. Walker, L. Baert, R. J. Wheeler, Proteins with proximal-distal asymmetries in axoneme localisation control flagellum beat frequency. bioRxiv, 2024.2005. 2008.593170 (2024).
83. S. M. King, Axonemal dynein arms. *Cold Spring Harb. Perspect. Biol.* **8**, a028100 (2016). doi: 10.1101/cshperspect.a028100; pmid: 27527589
84. M. E. Fowkes, D. R. Mitchell, The role of preassembled cytoplasmic complexes in assembly of flagellar dynein subunits. *Mol. Biol. Cell* **9**, 2337–2347 (1998). doi: 10.1091/mbc.9.9.2337; pmid: 9725897
85. G. R. Mali *et al*., Shulin packages axonemal outer dynein arms for ciliary targeting. *Science* **371**, 910–916 (2021). doi: 10.1126/science.abe0526; pmid: 33632841
86. K. Balasubramaniam, T. He, H. Chen, Z. Lin, C. Y. He, Cytoplasmic preassembly of the flagellar outer dynein arm complex in *Trypanosoma brucei*. *Mol. Biol. Cell* **35**, br16 (2024). doi: 10.1091/mbc.E24-06-0263; pmid: 39024276
87. C. Coutton *et al*., Mutations in CFAP43 and CFAP44 cause male infertility and flagellum defects in Trypanosoma and human. *Nat. Commun.* **9**, 686 (2018). doi: 10.1038/s41467-017-02792-7; pmid: 29449551
88. F. Shan, X. Yang, Y. Diwu, H. Ma, X. Tu, *Trypanosoma brucei* centrin5 is enriched in the flagellum and interacts with other centrins in a calcium-dependent manner. *FEBS Open Bio* **9**, 1421–1431 (2019). doi: 10.1002/2211-5463.12683; pmid: 31161731
89. Y. Wei, H. Hu, Z. R. Lun, Z. Li, Centrin3 in trypanosomes maintains the stability of a flagellar inner-arm dynein for cell motility. *Nat. Commun.* **5**, 4060 (2014). doi: 10.1038/ncomms5060; pmid: 24892844
90. K. K. Vasudevan *et al*., FAP206 is a microtubule-docking adapter for ciliary radial spoke 2 and dynein c. *Mol. Biol. Cell* **26**, 696–710 (2015). doi: 10.1091/mbc.E14-11-1506; pmid: 25540426
91. A. Ghanaeian *et al*., Integrated modeling of the Nexin-dynein regulatory complex reveals its regulatory mechanism. *Nat. Commun.* **14**, 5741 (2023). doi: 10.1038/s41467-023-41480-7; pmid: 37714832
92. H. T. Nguyen, J. Sandhu, G. Langousis, K. L. Hill, CMF22 is a broadly conserved axonemal protein and is required for propulsive motility in *Trypanosoma brucei*. *Eukaryot. Cell* **12**, 1202–1213 (2013). doi: 10.1128/EC.00068-13; pmid: 23851336
93. Z. P. Kabututu, M. Thayer, J. H. Melehani, K. L. Hill, CMF70 is a subunit of the dynein regulatory complex. *J. Cell Sci.* **123**, 3587–3595 (2010). doi: 10.1242/jcs.073817; pmid: 20876659
94. T. Fujiwara, C. Shingyoji, H. Higuchi, Versatile properties of dynein molecules underlying regulation in flagellar oscillation. *Sci. Rep.* **13**, 10514 (2023). doi: 10.1038/s41598-023-37242-6; pmid: 37386019
95. A. P. Carter, A. G. Diamant, L. Urnavicius, How dynein and dynactin transport cargos: A structural perspective. *Curr. Opin. Struct. Biol.* **37**, 62–70 (2016). doi: 10.1016/j.sbi.2015.12.003; pmid: 26773477

ACKNOWLEDGMENTS

We thank J. Stevens for assistance with DRC4 functional analysis experiments. We acknowledge the use of resources at the Electron Imaging Center for Nanomachines supported by UCLA and grants from the National Institutes of Health (NIH) and the National Science Foundation (NSF). **Funding:** This work was supported by the NIH (grant R01GM071940 to Z.H.Z., grant R01AI052348 to K.L.H., grant 1S10OD018111 to the EICN core facility, and grant R35 GM153408 to J.A.W.) and the NSF (grants DBI-1338135 and DMR-1548924 to the EICN core facility). **Author contributions:** Z.H.Z. and K.L.H. conceived the project and supervised research. X.X. prepared samples together with M.M.S., A.W., and H.W. X.X. recorded cryo-EM images, processed the data, and analyzed the structure. X.X. built the atomic models with help from S.L. and H.W. A.W., M.M.S., and G.L. generated and performed functional studies in mutant parasites. A.M.K. and J.A.W. performed proteomic analysis. X.X., K.L.H., Z.H.Z., and M.M.S. interpreted the results and wrote the manuscript. S.L. and H.W. edited the manuscript. All authors reviewed and approved the submitted manuscript. **Competing interests:** The authors declare no competing interests. **Data and materials availability:** Cryo-EM density maps have been deposited in the Electron Microscopy Data Bank under accession numbers EMD-47451 (48-nm repeat of wild type), EMD-47524 (96-nm repeat of wild type), EMD-47409 (48-nm repeat of *FAP106A*-KD), EMD-47410 (48-nm repeat of *FAP106B*-KD), and EMD-47411 (48-nm repeat of *PBP36*-KD). Atomic models have been deposited in the Protein Data Bank under accession numbers PDB:9E2G (48-nm repeat of wild type) and PDB:9E5C (96-nm repeat of wild type). All other data needed to evaluate the conclusions in the study are present in the main text or supplementary materials.

SUPPLEMENTARY MATERIALS

science.org/doi/10.1126/science.adr3314
Materials and Methods
Figs. S1 to S32
Tables S1 to S6
References (*96*–*137*)
Movies S1 to S4
Data S1
MDAR Reproducibility Checklist

Submitted 10 July 2024; resubmitted 11 November 2024
Accepted 6 January 2025
10.1126/science.adr3314